分类号 _____ 密级 _____

UDC _____ 编号 _____

中国科学院大学
理学博士学位论文

相对论重离子碰撞(RHIC)实验中双轻子的产生

赵杰

指导教师 马余刚 研究员

许怒 研究员

申请学位级别 理学博士 学科专业名称 粒子物理与原子核物理

论文提交日期 2013年4月 论文答辩日期 2013年5月

培养单位 中国科学院上海应用物理研究所

学位授予单位 中国科学院大学

答辩委员会主席 _____

Important Note

This is an English translation of part of Dr. Jie Zhao's Ph.D thesis. The full version can be found at:(https://drupal.star.bnl.gov/STAR/theses/phd-32). The current translation only includes the part(section: Analysis Technique) related to Au + Au $\sqrt{s_{NN}}$ = 200 GeV dielectron analysis based on the STAR data. If you have any concern please contact Jie Zhao (jiezhao1119@gmail.com).

Dielectron production at RHIC

Jie Zhao

Supervisor:

Prof. Yu-Gang Ma and Prof. Nu Xu

Shanghai Institute of Applied Physics
Chinese Academy of Sciences

April, 2014

Submitted in total fulfilment of the requirements for the degree of Ph.D. in Particle Physics and Nuclear Physics

目　录

目录 i

第一章 Introduction 1

第二章 RHIC-STAR experiment 3

第三章 Analysis Technique 5

3.1 Event selection 5

3.2 Electron identification 6

3.2.1 Electron selection 7

3.2.2 Electron purity and hadron contamination 9

3.3 Background reconstruction 11

3.3.1 Photon conversion 13

3.3.2 Event mixing 16

3.3.3 Mixed-event normalization 18

3.3.4 Like-sign background 21

3.3.5 Correlated background 25

3.3.6 Signal extraction 27

3.4 Efficiency and acceptance correction 28

3.4.1 Electron pair efficiency and acceptance 32

3.5 Hadronic cocktails 35

3.6 Systematic uncertainty 40

第四章 Results 45

第五章 Outlook 47

附录 A Appendix **49**

A.1 PHENIX acceptance 49

参考文献 **55**

Publication and presentations list **63**

第一章　Introduction

第二章　RHIC-STAR experiment

第三章　Analysis Technique

In this section i will discuss the detail of the dielectron analysis in 200GeV Au + Au collisions at RHIC-STAR. This chapter includes the following sections: Event selection, Electron identification, Background reconstruction, Efficiency and acceptance correction, Cocktail simulation, and systematic uncertainty.

3.1 Event selection

The data used in this analysis were collected by the Solenoidal Tracker At RHIC(STAR) detector in 2010, which contain two kinds of 200GeV Au + Au collision datasets: Minimum Bias trigger(MinBias) and Central trigger (Central) datasets. The MinBias trigger was defined as a coincidence in the east and west VPD(vertex position) detectors, and an online vertex cut to select collisions happening in the center of the detector. The Central triggered events were selected by requiring a small signal in the DC detectors as well as a large multiplicity from the barrel TOF, which corresponds to 0-10% of the total hadronic cross section.

We require the primary Vz to be centered within $30cm$ of the PC center to ensure the detector has a uniform acceptance. We also require the difference between primary vertexZ and the vertexZ from VPD(which is a fast trigger detector) to be less then $3cm$, in order to remove the pile-up background events(Fig. 3.1).

The centrality in Au+Au 200GeV collisions was defined using the uncorrected charged particle multiplicity ($dN/d\eta$) within $|\eta| < 0.5$. The $dN/d\eta$ distribution was then compared to a Monte Carlo(MC) Glauber calculation to define centrality bins. The dependence of $dN/d\eta$ on the collision vertex position Vz and the luminosity has been included to take the acceptance and efficiency change on the measured $dN/d\eta$ into account. Fig. 3.2 shows the measured uncorrected $dN/d\eta$ distribution in the region of $-5 < Vz < 5$ cm and extrapolated to zero ZDC coincidence rate for VPD triggered minimum bias events collected in year2010 Au+Au 200GeV in comparison to the MC Glauber calculation.

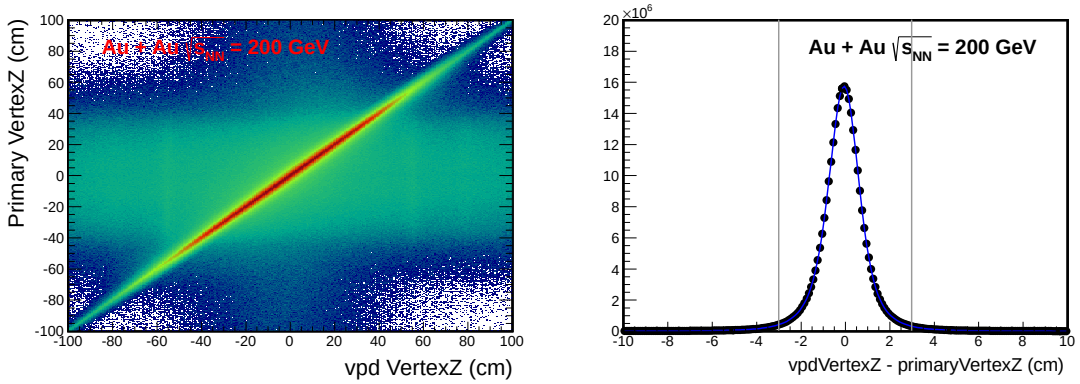

图 3.1: correlation between the primary vertex and the VPD vertex

These selection criteria yield 240M 0-80% minimum bias triggered and 220M central triggered (0-10%) Au+Au events at $\sqrt{s_{\rm NN}} = 200$GeV. Table.3.1 show the $\langle N_{\rm part}\rangle$ and $\langle N_{\rm coll}\rangle$ from Glauber calculation.

表 3.1: $\langle N_{\rm part}\rangle$, $\langle N_{\rm coll}\rangle$ from Glauber calculation($\sqrt{s_{\rm NN}} = 200$ GeV Au + Au)

Centrality	$\langle N_{\rm part}\rangle$	$\langle N_{\rm coll}\rangle$
0-10%	$325.9^{+5.4}_{-5.3}$	940^{+67}_{-70}
10-40%	$172.6^{+9.6}_{-9.0}$	393^{+49}_{-44}
40-80%	$41.5^{+7.0}_{-6.7}$	57^{+14}_{-14}
0-80%	$126.1^{+7.8}_{-6.5}$	293^{+36}_{-29}

3.2 Electron identification

In order to ensure good electron identification capability, in our analysis the electron tracks were required to satisfy the following selection cuts:

- number of fit points (out of 45) in the TPC greater than 20 to ensure good momentum resolution ($nHitsfit > 20$);
- the ratio of number of fit points over number of possible points greater than 0.52 to avoid split tracks in the TPC ($nHitsfit/nHitsposs > 0.52$);

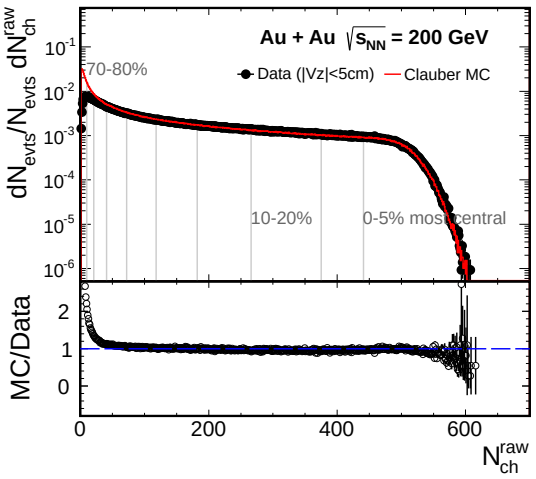

图 3.2: uncorrected charged particle multiplicity compare with Glauber calculation

- distance of closest approach (dca) to the primary vertex less than 1 cm to select tracks from primary collisions ($dca < 1cm$);
- number of dE/dx points used for calculating dE/dx greater than 15 to ensure good dE/dx resolution ($ndEdxhits > 15$);
- with a valid matching to a TOF hit;
- projected position on the TOF module within the sensitive readout volume. ($|yLocal| < 1.8cm$).

3.2.1 Electron selection

Electrons (including positions if not specified) were identified with a combination of the TPC and TOF detectors. In low multiplicity collisions, by requiring a TOF velocity cut, electrons can be cleanly separated from hadrons in the TPC dE/dx vs. momentum (p) plot. However, the situation becomes a bit complicated in high multiplicity Au+Au collisions. Figure 3.3 shows the normalized dE/dx - $n\sigma_e$ vs. p distributions from Au+Au 200 GeV collisions for all charged particles (upper panel) and for charged particles after implementing a TOF velocity cut

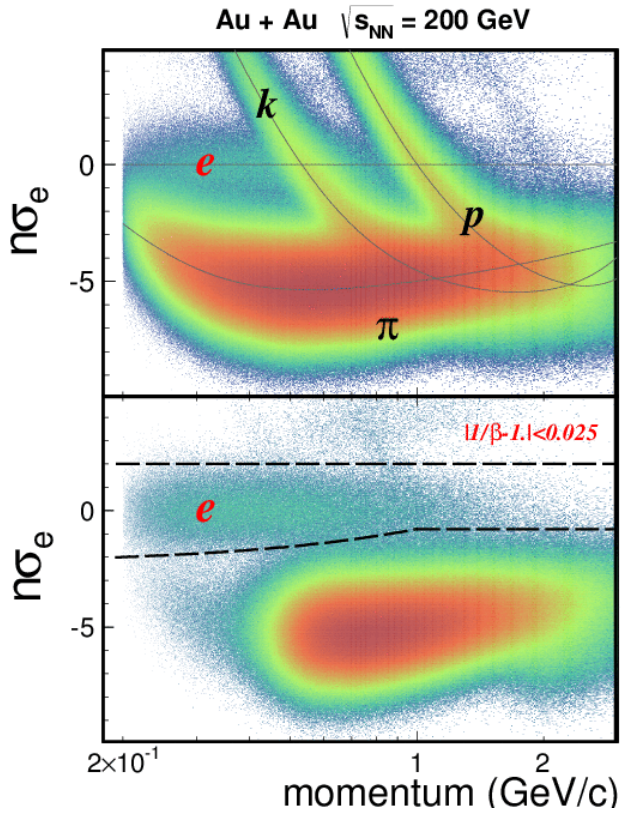

图 3.3: Upper Panel: normalized dE/dx - $n\sigma_e$ vs. momentum (p) distributions for all charged particles. Bottom Panel: $n\sigma_e$ vs. p distribution after applying a TOF velocity cut $|1/\beta - 1| < 0.025$.

$|1/\beta - 1| < 0.025$ (lower panel, and this cut will accept about 95% of electron based on the TOF timing resolution). The $n\sigma_e$ is defined as:

$$n\sigma_e = \frac{\ln \frac{\langle dE/dx \rangle^{\rm mea}}{\langle dE/dx \rangle_e^{\rm th}}}{R_{dE/dx}} \tag{3.1}$$

where the subscripts of 'mea' and 'th' are measured and theoretical values, respectively. $R_{dE/dx}$ is the experimental dE/dx resolution. One can see after the TOF velocity selection, there are still some slow hadrons contributing to the electron band in this distribution.

Figure 3.3 is plotted for each association between TOF hits and TPC charged

tracks. For most cases that TOF hits are correctly associated with the originated charged particles, then one would have a meaningful particle velocity measurement that can be used for further particle identification. There are also many TOF hits that are fired by photon conversion electrons generated from the material between TPC and TOF sensitive detector volumes. Photons don't leave trajectories in the TPC. However, these hits can be randomly associated with charged particle tracks in the TPC in high multiplicity event. Figure 3.4 upper panel shows the inverted particle velocity ($1/\beta$) measured by the TOF vs. the particle momentum (p) measured by the TPC for all TPC-TOF associations in Au+Au collisions at $\sqrt{s_{\rm NN}} = 200\,{\rm GeV}$. The band below 1 depicts those associations between conversion electron TOF hits and random TPC charged tracks. Figure 3.4 bottom panel shows the $1/\beta$ distributions in the momentum range $0.2 < p < 0.25\,{\rm GeV}/c$ for three centrality classes. Three distributions are normalized at the pion peak. One can see with increasing multiplicity, the fake association fraction increases dramatically.

The consequence of this effect is that when requiring a particle velocity cut to be close to the speed of light, one can still include some of these random associated charge hadron tracks, mostly at ~ 400 MeV/c above. These hadrons remain in the dE/dx vs. p distribution in Fig. 3.3 lower panel, which introduces additional hadron background in the selected electron candidates in the region where electron dE/dx band crosses with hadrons (mostly kaons and protons). In Fig. 3.3 lower panel, solid black lines depict the dE/dx cuts to select single electron candidates in this analysis.

3.2.2 Electron purity and hadron contamination

The $n\sigma_e$ vs. p distribution after the TOF velocity cut has been shown in Fig. 3.3. We performed a multi-component fit to the $n\sigma_e$ distribution in each momentum slice to decompose yields of each particle species, and thus to derive the electron purity and hadron contamination under a certain $n\sigma_e$ cut. The $n\sigma_e$ distribution for electrons is assumed to be gaussian, and its position and shape was determined by selecting π^0 Dalitz decay electrons and conversion electrons using invariant mass reconstruction(Fig. 3.5left). The positions and shapes

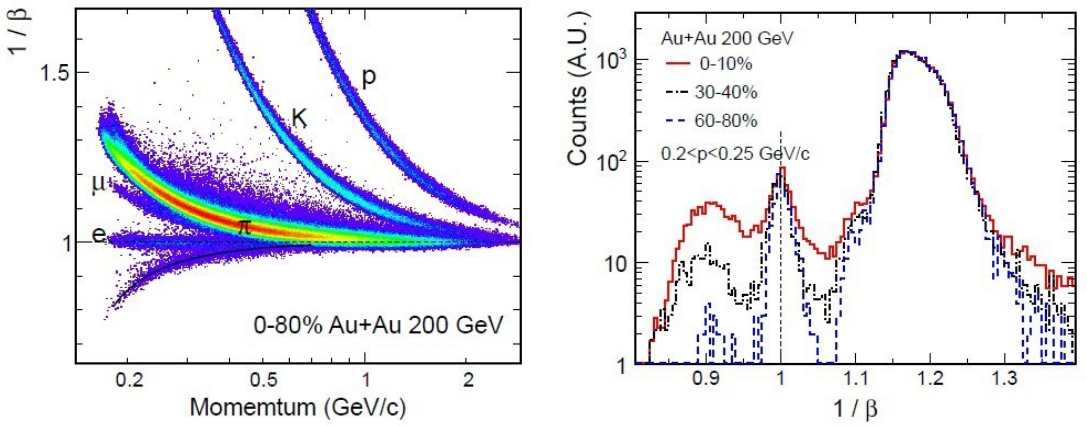

图 3.4: Upper Panel: $1/\beta$ vs. particle momentum. Solid line depicts a prediction for those associations that TOF hits were triggered by conversion electrons while matched randomly with TPC charged tracks. Bottom Panel: $1/\beta$ projection in the momentum bin $0.2 < p < 0.25\,\mathrm{GeV}/c$ for three centrality bins, normalized in the pion peak region.

of $n\sigma_e$ distributions for pions, kaons and protons were determined by selecting pure samples of these particles with the particle mass calculated from TOF(Fig. 3.5right). We fixed the positions and shapes of all components, leaving only the yields of each as free parameter to fit the $n\sigma_e$ distribution in Fig. 3.3.

We fit the $n\sigma_e$ distribution in each momentum region to estimate the electron purity. The $n\sigma_e$ shapes of π, K, p and e are from the selected high purity sample. Only the particle yield are the free parameters. This makes the fitting much easier to control compare to the multi-gaussian fit with open free parameters. Fig. 3.6 upper left plots show the $n\sigma_e$ distribution for each components, and the left bottom panel is the fitting to the total $n\sigma_e$ distribution. Fig. 3.6 right plot shows the estimated electron purity vs momentum, and the total electron purity can be found in Table. 3.2.

MinBias:	$0.946 + / - 0.023$
Central:	$0.921 + / - 0.025$

表 3.2: electron purity

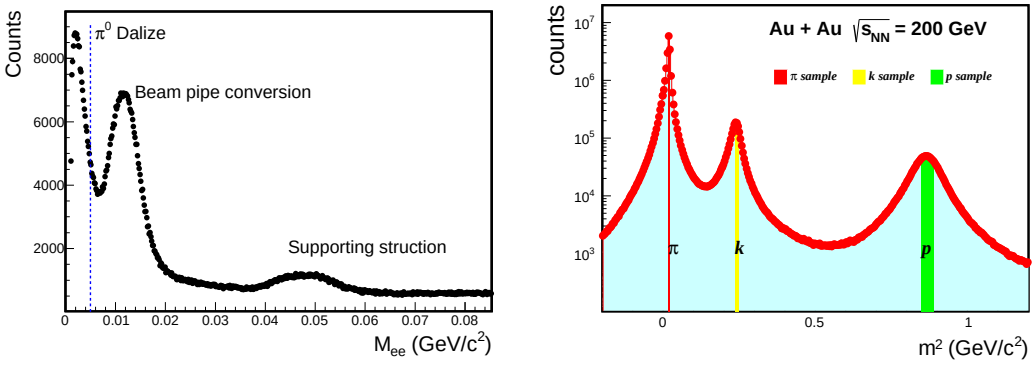

图 3.5: (Left)invariant mass reconstruction of the π^0 Dalitz decay electrons and conversion electrons，(Right)TOF $mass^2$ cut for high purity hadron sample.

3.3 Background reconstruction

All electron and position candidates with $p_T > 0.2GeV/c$ and $|\eta| < 1$ from the same event are combined to generate the foreground unlike-sign pair N_{+-} invariant mass distribution. The N_{+-} contain the signal and background, the signal means particle decayed dielectrons and the pair production from QGP/medium. the background includes:

- Combinatorial background pairs from randomly combining two uncorrelated electrons.
- Correlated background pairs. For instance, in the case of Dalitz decays followed by a conversion of the decay photon(e.g., $\pi^0 \to e^+e^-\gamma$, then $\gamma Z \to e^+e^-Z^*$), the electron from the Dalitz decay and the positron from the conversion are not completely uncorrelated as they are originated from the same source. Another significant contribution is the electron pairs from the same jet fragmentation or back-to-back di-jet fragmentation. This source may become more significant at high mass or p_{T}.

To calculate contributions of uncorrelated and correlated background, we constructed like-sign pairs N_{++}, N_{--} from the same event. It has been demonstrated when the e^+ and e^- are produced in statistically independent pairs, the

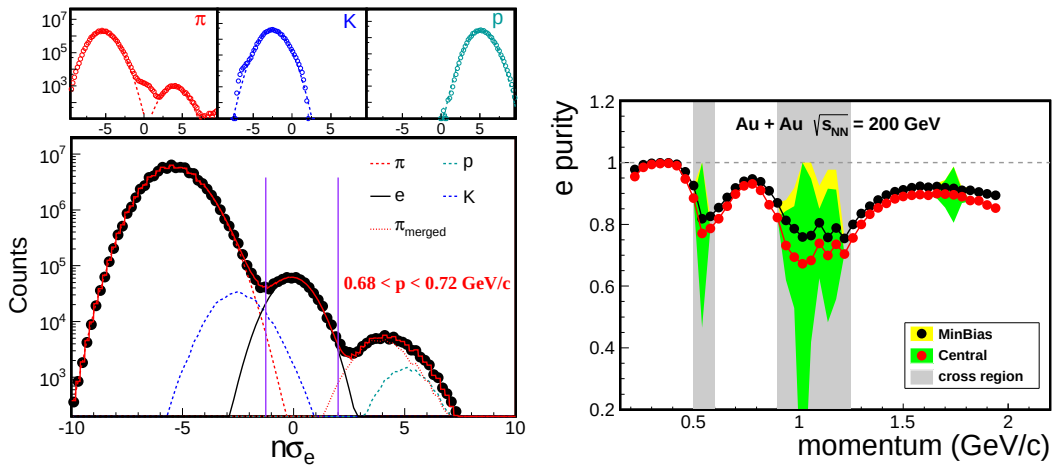

图 3.6: (Left)$n\sigma_e$ distribution in certain momentum region，(Right)electron purity estimation for

geometric mean of the like-sign pairs $2\sqrt{N_{++} \times N_{--}}$ fully describes the background in the unlike-sign pair foreground distribution N_{+-} [45]. In this analysis, we always used the like-sign distribution $2\sqrt{N_{++} \times N_{--}}$ to estimate or justify the background distribution. The mixed-event unlike-sign distribution B_{+-} was explored to estimate the combinatorial background, and it was used for background estimation wherever the correlated background is negligible or the mixed-event unlike-sign distribution agrees with the same-event like-sign distribution $2\sqrt{N_{++} \times N_{--}}$ for better statistics. Mixed-event like-sign pair distributions B_{++} , B_{--} were constructed as well to justify the applicable kinematic region for the mixed-event technique as well as to define the normalization factor for the mixed-event unlike-sign distribution.

These two methods have their own advantages: the like-sign method can reproduce both the combinatorial and corrected background, but the statistics is in the same order as the same-event unLike-sign itself, and another important thing for like-sign method is that it need to be corrected the acceptance difference for like and unlike sign pairs. For mix-event background, as we can increase statistics as we can, so the statistics are much lager compare to like-sign method, and there is no need to correct for the acceptance. However, it can’ t reproduce

the correlated background. We combined these two methods in our background reconstruction, detail will be discussed in the following parts.

Figure 3.7 show the two-dimensional (M_{ee} vs p_{ee}^{T}) $e^{+}e^{-}$ signal in 200 GeV Au + Au minimum bias (0-80%) collisions, which clearly show vector meson(ω, ϕ, J/ψ) signals.

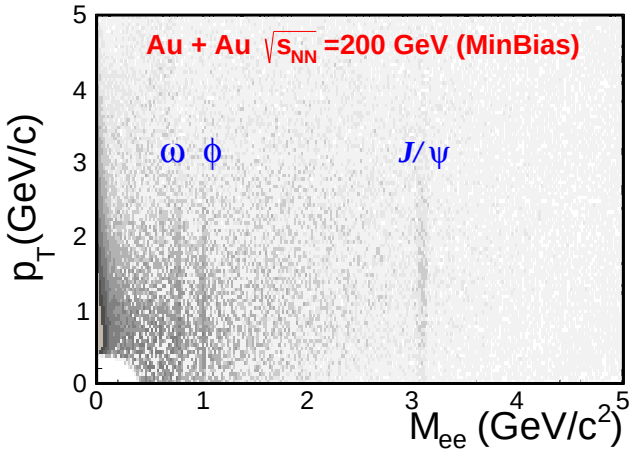

图 3.7: Two-dimensional (M_{ee}, p_{T}) distribution of $e^{+}e^{-}$ signal from 200 GeV Au + Au minimum bias (0-80%) collisions in the STAR acceptance ($p_{\mathrm{T}} > 0.2\,\mathrm{GeV}/c$ and $|\eta| < 1$) and $|y_{ee}|$ <1.

3.3.1 Photon conversion

There are $e^{+}e^{-}$ background from the photon conversions, which are the contribution from the photons interacting with the detector material and converted into electron pairs. we use two method to remove the photon conversion: ϕ_V cut and pair mass cut methods.

In our analysis, the ϕ_V cut method used to remove the photon conversion is similar as that used by the PHENIX collaboration [45]. The idea is the opening angle between the two conversion electrons should be zero, and the electron tracks are bent only in the plane perpendicular to the magnetic field direction, which is parallel to the beam axis z in STAR. We inherited the same definition for the following unit vectors and defined the angle ϕ_{V} as:

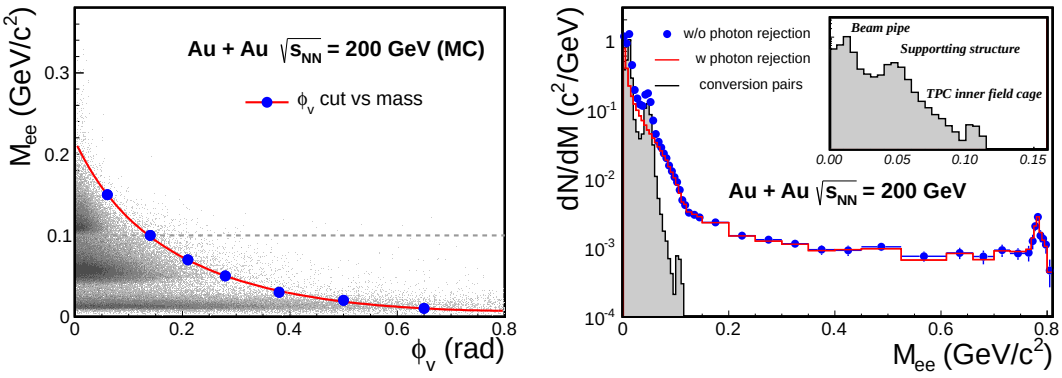

图 3.8: Left Panel: ϕ_V vs mass distributions for photon conversion electron pairs form the full GEANT MC simulation. The solid red line depicts the mass dependent ϕ_V cut that was used to remove these conversion pairs. Right Panel: photon conversion contribution in 200 GeV Au + Au collisions. The insert plot shows the structures from beam pipe, supporting bars of inner cone and TPC inner field cage.

$$\begin{aligned} \hat{u} &= \frac{\vec{p}_+ + \vec{p}_-}{|\vec{p}_+ + \vec{p}_-|}, \hat{v} = \vec{p}_+ \times \vec{p}_- \\ \hat{w} &= \hat{u} \times \hat{v}, \hat{w}_c = \hat{u} \times \hat{z} \\ \cos\phi_V &= \hat{w} \cdot \hat{w}_c \end{aligned} \tag{3.2}$$

where $\vec{p}_+$, $\vec{p}_-$ are momentum vectors of $e^\pm$ tracks, and $\hat{z}$ is the magnetic field direction.

For pairs originated from photon conversions ϕ_V should be zero. It has no preferred orientation for combinatorial pairs, and very weak dependence for e^+e^- pairs from hadron decays. Figure 3.8 left panel shows the electron pair mass vs. ϕ_V for conversion electron pairs from the full GEANT simulation with the appropriate STAR detector geometry [59]. The populated bands at different mass positions depict the conversion electron pairs from different detector materials. Their masses are shifted a bit from zero because in the tracking algorithm we forced these tracks whose *dca*s are close to the primary collision vertex to originate from the primary vertex exactly. The three main bands from low to high masses

correspond to the conversions from the beam pipe (at a radius r of $\sim$ 4 cm), inner cone support structure ($r \sim 20$ cm) and TPC inner filed cage (IFC) ($r \sim$ 46 cm). We define a mass dependent ϕ_V cut shown as the red line in order to remove these conversions. We estimated that more than 95% conversion pairs can be removed by the cut from the simulation.

Figure 3.8 right panel shows the signal pair invariant mass spectra before (blue dots) and after (red histogram) this photon conversion rejection cut and the difference is shown as the filled histogram. Like-sign background subtraction was used to obtain these distributions. We can see that almost all conversions appear in the mass region below 0.1 GeV/c^2. We consider another method to remove the photon conversion contribution - pair mass cut method, which remove all of the electron pairs with the pair mass less then 0.1 GeV/c^2, in this way both the conversion and the π^0 Dalitz decay contribution are removed.

In the dielectron analysis, most of electrons are coming from the photon conversion or the π^0 Dalitz decay, the removal of the conversion/Dalitz decay electrons will reduce the combinatorial background, and increase the S/B, but it also has some effect on the dielectron reconstruction efficiency(Fig. 3.9), so we compare the results from different method, and took the difference into the systematic uncertainty.

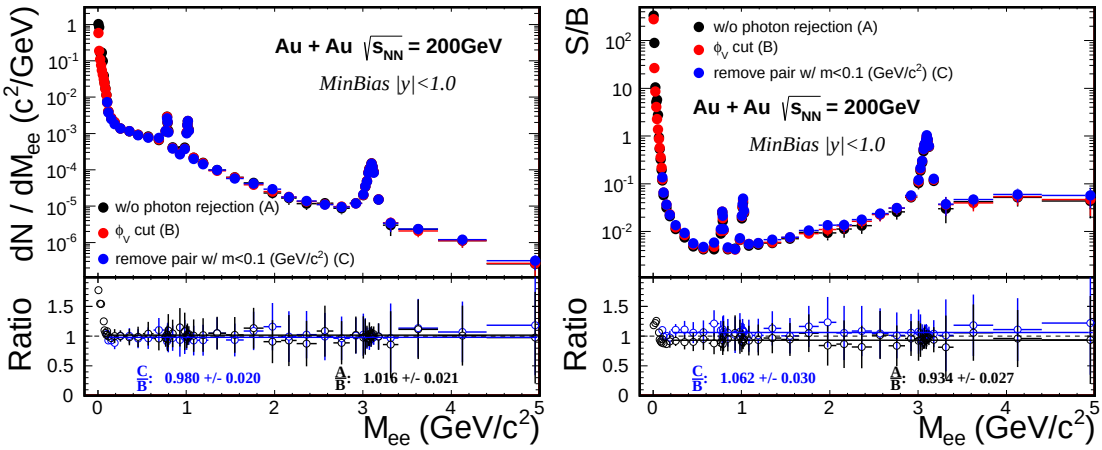

图 3.9: Results from different conversion rejection method, and the S/B ratio.

3.3.2 Event mixing

The event mixing technique is used to reproduce the combinatorial background, which combine tracks from different events with definitely no correlation. As the general property of the tracks from different event are not the same, in order to make it much more comparable to the same event. We divide the dataset in several event pools by some general event level property, like reference multiplicity, primary vertexZ, eventplane and the magnetic field direction, and combine the tracks from the same event pool to do the event mixing.

The technique used to divide the event pool with different vertex, reference multiplicity has been widely used in the STAR analysis [69], which is to ensure the detector has a uniform acceptance, and similar efficiency.

From the previous RHIC flow measurements, we know there is a large asymmetry in the final particle momentum space, so we need to consider the eventplane direction effect to ensure the events mixed have similar momentum space(Fig 3.10).

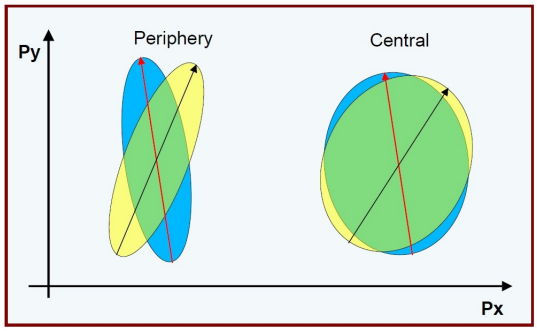

图 3.10: Momentum anisotropies in peripheral(large flow) and central events(small flow).

The event plane was reconstructed with the conventional event plane method with tracks in the TPC ($0.1 < p_{\mathrm{T}} < 2\,\mathrm{GeV}/c$ and $|\eta| < 1$) to obtain the second order event plane angle Ψ [70]. Figure 3.11 shows a study of comparing mixed-event unlike-sign and like-sign distributions using different number of event pools in event plane angle in minimum bias Au + Au collisions. The figure shows several different scenarios from 1 up to 24 event pools. The dashed lines show

±0.5% difference, or in another expression 100% change in the signal yield when signal-to-background ratio is 1/200. This study shows that if we don't do the division in event plane angle, the mixed-event distributions will be distorted. The distortion is quite clear in the low mass region ($< 1\,\mathrm{GeV}/c^2$), and not negligible in the intermediate mass region ($1-3\,\mathrm{GeV}/c^2$). When the number of event pools is above 12, the differences become negligible. The number is also reasonably consistent with our TPC 2nd order event plane resolution, which is about 0.8 in 200 GeV Au + Au minimum bias collisions. We further studied its centrality dependence. To ensure the minimal difference in all centrality bins we will report, we choose 24 event pools in the event plane angle in our analysis.

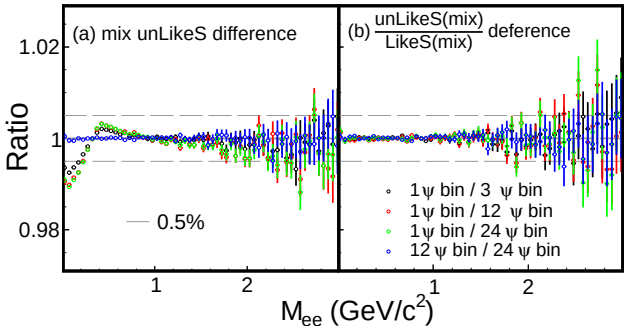

图 3.11: Difference in mixed-event distributions when using different number of event pools in the reconstructed event plane angle. The left plot shows differences of unlike-sign distributions with different divisions and the right plot shows differences of ratios of unlike-sign to like-sign distributions.

The data sample used in this analysis were taken under two different magnetic field configurations (same magnitude but opposite directions) due to the TPC calibration reasons. Acceptance of opposite charged tracks in two opposite magnetic fields is not exactly the same due to the slight offset of the beam line w.r.t. to the center of STAR detector system. We then only mixed those events with the same magnetic field configuration when constructing total mixed-event distributions.

Finally, the number of event pools used in multiplicity, vertex position, event plane angle and magnetic field configuration in this analysis is $16 \times 10 \times 24 \times 2$

for 200 GeV minimum bias Au + Au collisions.

The statistics in the mixed-event distributions depends on the number of events chosen for the calculation. Typically one would like to have this number as large as possible to minimize the statistical uncertainty in the mixed-event distributions. However, given a finite data sample, with sizable number of event pools, one need to make sure that the mixed-event calculation is done sufficiently in every event pool. Figure 3.13 shows the differences between mixed-event distributions with different number of events in buffer for mixed event calculation. We can see up to 50 number of events in buffer, there is no distortion in the measured mixed-event distributions beyond statistics. We chose 50 events in buffer in our calculation, and the statistical uncertainties in mixed-event are negligible compared to the same event distributions.

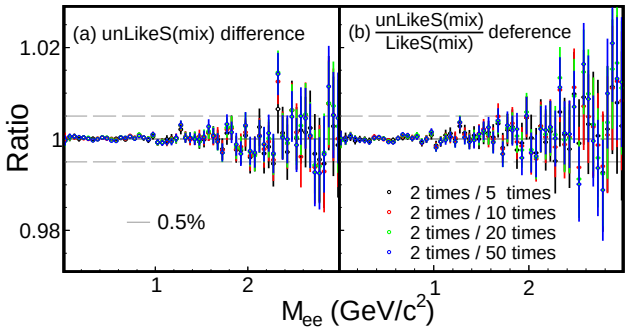

图 3.12: Buffer size dependence of the mixed-event distributions.

Every events are included in the event mixing to avoid bias when combine the spectra from different event pools, as both the signal and background shape may be different in each event pool. e.g. centrality dependence.In this way the mixed event will follow the same possibility of the same event in each event pool Fig. 3.13.

3.3.3 Mixed-event normalization

We constructed the unlike-sign and like-sign pair distributions in the same event - N_{+-}, $N_{\pm\pm}$ and in the mixed-event - B_{+-}, $B_{\pm\pm}$ distributions in the two dimension (M_{ee}, p_{T}) plane. The mixed-event unlike sign distribution B_{+-} will

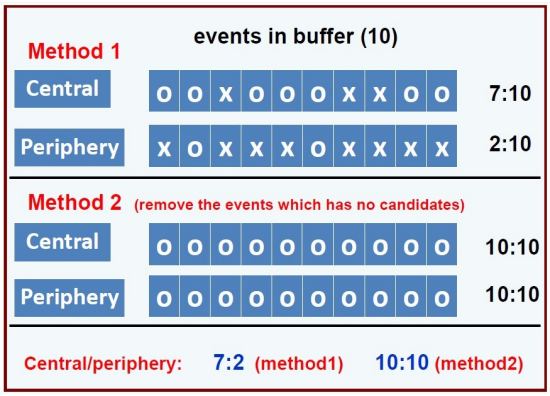

图 3.13: Buffer events filling method.

provide the uncorrelated combinatorial background shape. However, the overall normalization factor for this distribution need to be properly calculated. We used the same technique as described in Ref. [45] which used the like-sign pair distributions (with no signal) to determine the normalization factor. One important factor is that the same-event like-sign pairs also have the contributions from correlated pairs. A proper kinematic region ought to be carefully selected where the correlated background is negligible.

The procedure to obtain the normalized combinatorial background $B_{+-}^{\rm comb}$ is described in Ref. [45] and also shown in the following Eq. 3.3:

$$
\begin{aligned}
A_+ &= \frac{\int_{\rm N.R.} N_{++}(M,p_T)dMdp_T}{\int_{\rm N.R.} B_{++}(M,p_T)dMdp_T} \\
A_- &= \frac{\int_{\rm N.R.} N_{--}(M,p_T)dMdp_T}{\int_{\rm N.R.} B_{--}(M,p_T)dMdp_T} \\
B_{++}^{\rm norm} &= \int_0^\infty A_+ B_{++}(M,p_T)dMdp_T \\
B_{--}^{\rm norm} &= \int_0^\infty A_- B_{--}(M,p_T)dMdp_T \\
B_{+-}^{\rm comb}(M,p_T) &= \frac{2\sqrt{B_{++}^{\rm norm}\cdot B_{--}^{\rm norm}}}{\int_0^\infty B_{+-}dMdp_T} B_{+-}(M,p_T)
\end{aligned}
\tag{3.3}
$$

Figure 3.14 upper panel shows the residual difference between same event like-sign $N_{\pm\pm}$ and the normalized mixed-event $B_{\pm\pm}^{\rm norm}$ as a function of M_{ee} and $p_{\rm T}$.

The difference is normalized by the expected statistical error in each kinematic bin. The bottom panel shows the residual difference distributions for all entries in different mass regions. One can see in the black box area the normalized residuals follow the statistical fluctuation. We then chose this area $1 < M_{ee} < 2\,\mathrm{GeV}/c^2$ as the normalization region in our analysis. As one of the systematic uncertainty source on the normalization factor, we used different normalization regions for calculation and details will be discussed in the following part.

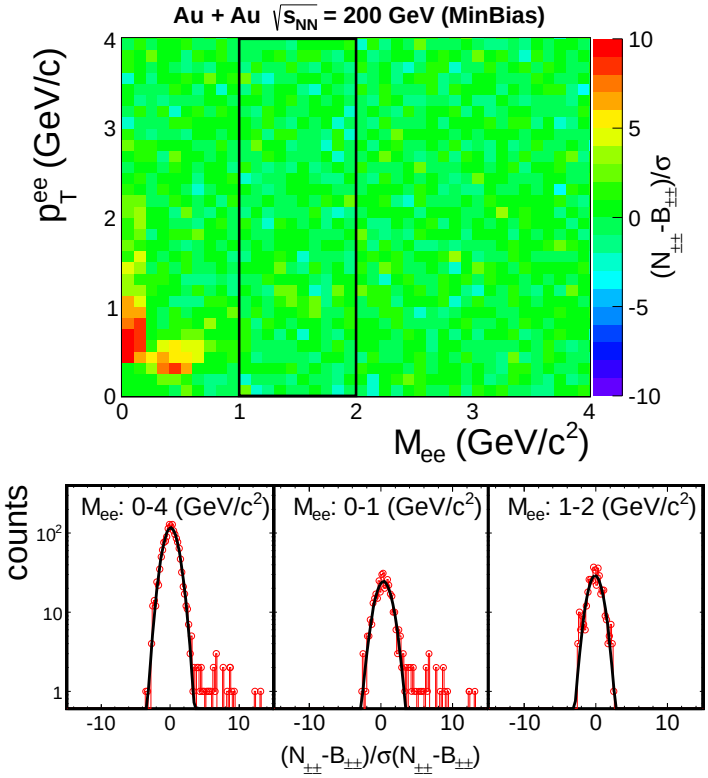

图 3.14: Upper panel: Residual difference between same event and mixed events like-sign distributions divided by its standard deviation. The black box indicated the default normalization region. Bottom Panel: Residual difference distributions for all the entries in different mass regions.

Table 3.3 lists the total like-sign pairs in the normalization region (N.R.) in each centrality class and the corresponding relative statistical uncertainties.

The raw mass distributions of mixed-event like-sign and unlike-sign pairs

表 3.3: Total Like-sign pairs in the normalization region (N.R.) in each centrality class and the corresponding relative statistical uncertainties.

Centrality	Like-sign pairs in N.R.	Statistical uncertainty
0-80%	3.70×10^7	1.6×10^{-4}
0-10%	8.05×10^7	1.1×10^{-4}
10-40%	2.10×10^7	2.2×10^{-4}
40-80%	2.67×10^6	6.1×10^{-4}

in the full p_T region are plotted in Fig. 3.15(left) together with the same event distributions. To further investigate any residual difference between these distributions, ratios between them are plotted in Fig .3.15(right). In the low mass region we can see the contribution from the cross pairs. Panel (a-c) show in the normalization region, the residual is negligible. The potential increasing trend at high mass region can be attributed to the possible jet correlated background [45]. This will be discussed further in systematic uncertainty part.

3.3.4 Like-sign background

The like-sign distribution is taken as the right description for the background in the unlike-sign foreground distribution. However, there is some acceptance difference between the like-sign and the unlike-sign pairs in our detector system sitting inside a magnetic field. Figure 3.16 shows our observed candidate e^+ and e^- tracks ϕ vs. p_{T}. The empty strips along the ϕ direction are due to the TPC read-out sector boundaries. In the active detecting area, small local inefficiencies or acceptance holes will result in different acceptance for like-sign and unlike-sign pairs. We used the mixed-event technique to calculate this acceptance difference.

The ratio obtained with mixed-event distributions was used to correct for the acceptance difference in the same event like-sign distribution to account for the unlike-sign background. The ratio was calculated in each (M, p_{T}) bin, and applied in this 2D plane. The geometric mean from two like-sign charge combinations ++, −− describes exactly the background in +− in total pairs in spite of any detecting efficiency. When calculating the combined like-sign pair in each

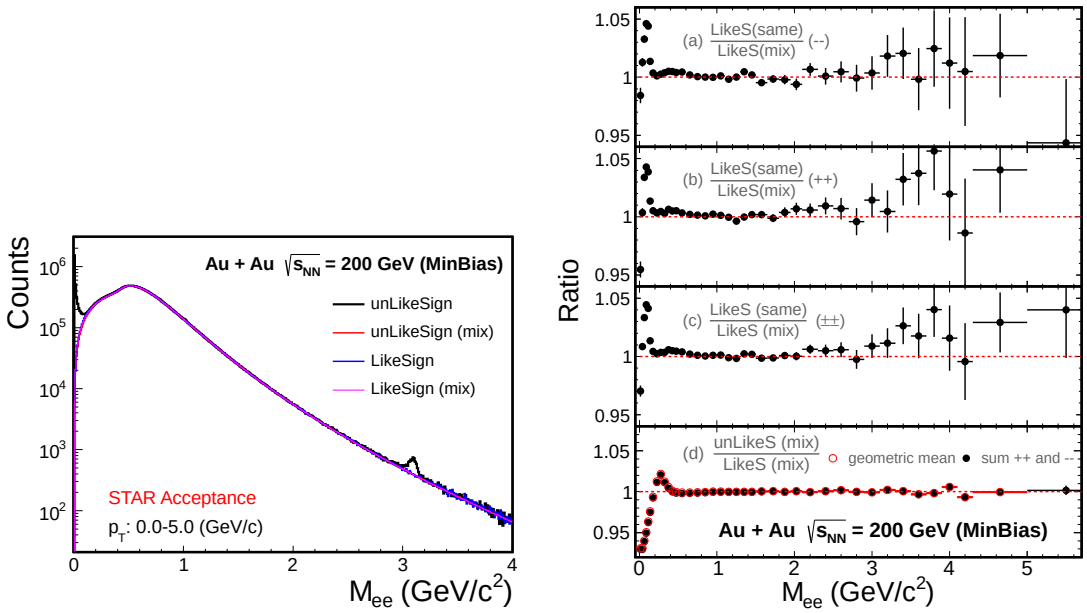

图 3.15: (Left)Raw pair mass distribution for 200 GeV Au + Au collisions. (Right)(a), (b), (c) Ratios between same event and mixed-event like-sign distributions and (d) Ratio of mixed-event unlike-sign and like-sign distributions in 200 GeV Au + Au minimum bias collisions.

kinematic bin, we used both geometric mean and the direct sum of ++ and −− in the calculation to estimate the impact of potential asymmetric detecting efficiencies for positive and negative tracks, shown in Eq. 3.4.

$$
\begin{aligned}
N^{\mathrm{corr}}_{\pm\pm}(M,p_T) &= 2\sqrt{N_{++}(M,p_T)\cdot N_{--}(M,p_T)}\ \cdot \boxed{\frac{B_{+-}(M,p_T)}{2\cdot\sqrt{B_{++}(M,p_T)\cdot B_{--}(M,p_T)}}} \\
N^{\mathrm{corr}}_{\pm\pm}(M,p_T) &= a[N_{++}(M,p_T)+N_{--}(M,p_T)]\ \cdot \boxed{\frac{B_{+-}(M,p_T)}{b\cdot[B_{++}(M,p_T)+B_{--}(M,p_T)]}} \\
a &= \frac{\int_0^\infty 2\cdot\sqrt{N_{++}(M,p_T)\cdot N_{--}(M,p_T)}dMdp_T}{\int_0^\infty[N_{++}(M,p_T)+N_{--}(M,p_T)]dMdp_T} \\
b &= \frac{\int_0^\infty 2\cdot\sqrt{B_{++}(M,p_T)\cdot B_{--}(M,p_T)}dMdp_T}{\int_0^\infty[B_{++}(M,p_T)+B_{--}(M,p_T)]dMdp_T}
\end{aligned}
\tag{3.4}
$$

Figure 3.17 shows the ratio of mixed-event unlike-sign and like-sign distri-

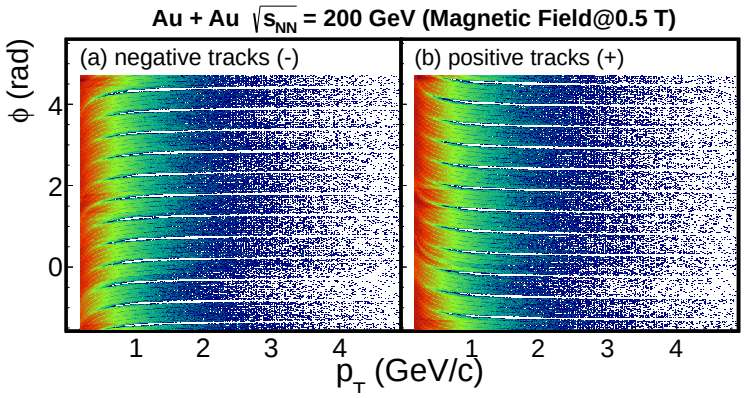

图 3.16: ϕ vs p_T for all negative (left) and positive (right) tracks from single magnetic field configuration. The blank areas are due to the TPC sector boundaries, which shows the different acceptance between positive and negative tracks particularly in the low p_T due to the magnetic field.

butions vs the pair mass integrated over all p_T region. The like-sign pairs were calculated using the geometric mean of two charge sign combinations. The structure at low mass region was understood to be caused by local inefficiencies and acceptance holes. This ratio has a dependence on the pair p_T and eventually the correction was applied to the like-sign distributions in the 2D (M, p_{T}) plane.

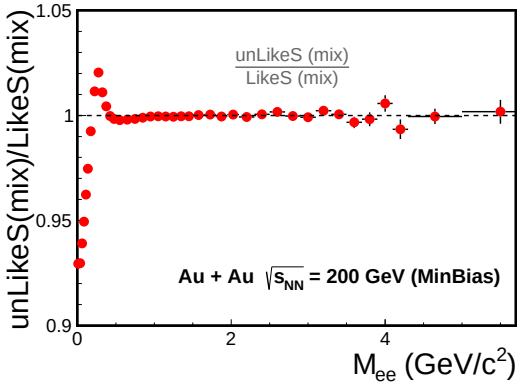

图 3.17: Acceptance correction factor for unlike-sign and like-sign pair difference from 200 GeV Au + Au minimum bias collisions.

Both like and unlike sign are effected by the acceptance, so the unlike sign

itself also need to correct, this correction estimated by MC simulation, and as the effect is small($< 1\%$), we folded it into the efficiency calculation(p_T, η, ϕ) (Fig. 3.18).

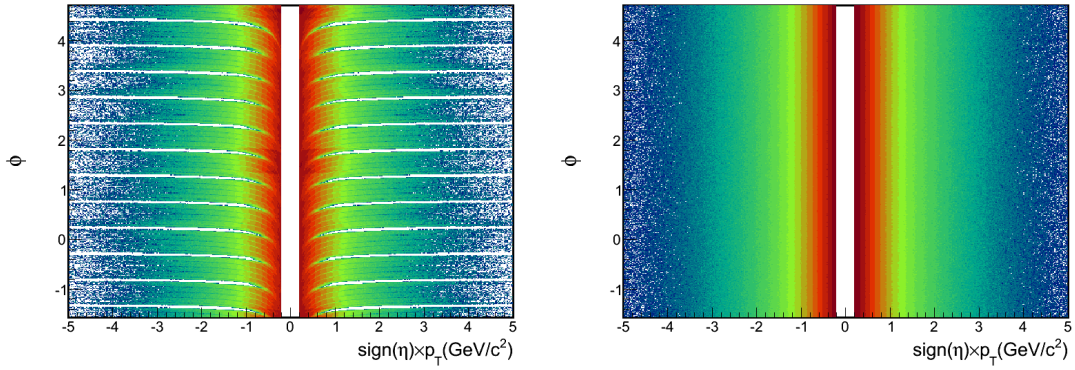

图 3.18: simulated single track acceptance for STAR acceptance(left) and Full ϕ acceptance (right), the momentum distribution and η distribution are from realdata.

The mixed-event method cannot fully reproduce the pair inefficiency in the same event due to the detector cluster hit merging. The loss effect is different for like-sign and unlike-sign pairs in a magnetic field. This effect can come from the TPC track merging or the TOF hit merging.

We used two particle correlation to study this acceptance loss effect due to the TPC track merging. We calculated the $\Delta\eta$ and $\Delta\phi$ correlation of like-sign and unlike-sign pairs in both same and mixed event. As a conservative estimation, we artificially removed a significant amount of detecting area near (0,0), and corrected the background subtracted spectra with the cut efficiency which was estimated by the mixed-event(Fig. 3.19). We observed the difference on the final mass spectrum is $<1\%$. In the real situation, the TPC hit resolution is around 1 mm, the expected acceptance hold due to the merging is significantly smaller than what we estimated here. We then concluded the effect due to the TPC track merging is negligible(Fig. 3.20).

Similarly, this loss effect can happen when two TPC tracks are pointing to the same TOF read-out cell (size 6×3 cm^2). The TOF matching algorithm will

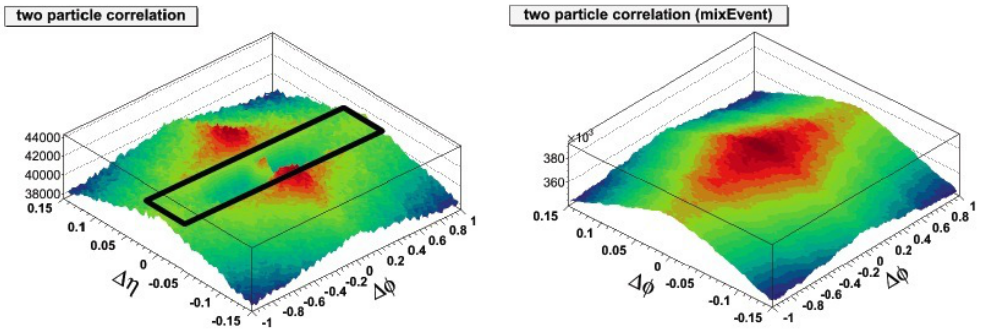

图 3.19: Two particle correlation in same event and mix event, the black box are the region which cause by track merge

remove any TPC-TOF association in this situation since it cannot resolve the timing of two close hits. We also artificially removed pairs with TOF hits in the neighboring cells (thus the acceptance hole is increased by about a factor of 9). We found the impact on the final acceptance correction factor is <0.2%, and only in some particular mass region(Fig. 3.21).

3.3.5 Correlated background

In this analysis, we always took the like-sign distribution as a full description of the background in the foreground unlike-sign distribution. The mixed-event unlike-sign distribution after properly normalization produced the combinatorial background contribution. We then took the difference between the like-sign and the mixed-event unlike-sign to understand the correlated background contributions.

Figure 3.22 shows the ratio of the acceptance corrected like-sign to the mixed-event unlike-sign distributions. In the low mass region ($< 1\,\mathrm{GeV}/c^2$), the difference is due to the cross pair contributions like $\pi^0 \rightarrow e^+e^-\gamma$, then $\gamma Z \rightarrow e^+e^-Z^*$ etc. In the intermediate and high mass regions, the like-sign and mixed-event distributions generally agree within our current precision, but also shows a trend of increasing excess vs. mass. This is mostly due to the back-to-back jet correlation.

We then used a data-driven method to estimate the correlated background

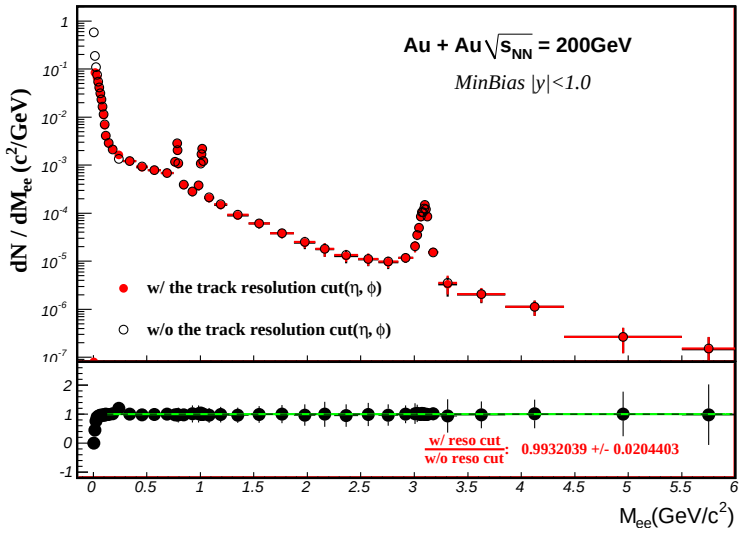

图 3.20: The difference with and without consider the track merge effect.

contribution. We fit the ratio in Fig. 3.22 in the mass region above 1 GeV/c^2 with a few different empirical functions: 2nd order polynomial and exponential etc. We counted this difference, although small, as the residual correlated background contribution. We used the 95% confidence limits from the fit (indicated by the dashed lines in the figure) as the systematic uncertainty on the correlated background. The lower limit of this uncertainty is consistent with unity, where the like-sign background is consistent with the mixed-event unlike-sign background.

This residual background has been studied in different p_T and different centrality bins. Figure 3.23 shows the p_T and centrality dependence of the unlike-sign foreground and mixed-event mass distributions. And Fig. 3.24 shows the acceptance correction ratio, which was estimated via the ratio between unlike-sign and like-sign mixed-event distributions, and the ratio of acceptance corrected like-sign background to mixed-event unlike-sign distributions in various p_T and centrality selections. The acceptance correction factor shows a slight centrality dependence as the number of electron candidates is different in each centrality. It has a strong p_T dependence due to different track curvatures in different p_T in the magnetic field. At sufficient high p_{T}, tracks almost go as straight lines, therefore

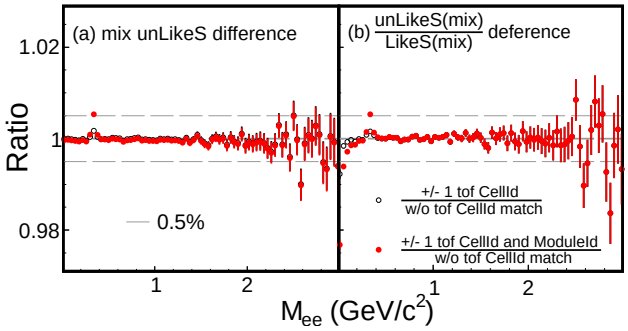

图 3.21: TOF matching effect for pair reconstruction

the acceptance for like-sign and unlike-sign pairs should be similar. The similar data-driven procedure has been pursued to estimate the correlated background in each p_T and centrality bin.

3.3.6 Signal extraction

In our analysis, we directly subtracted the like-sign from the foreground unlike-sign distribution in the mass region of $M_{ee} < 0.75\,\mathrm{GeV}/c^2$. While at higher mass region, we firstly subtracted the combinatorial background using the mixed-event unlike-sign pairs for the better statistics. For the residual correlated background, we used the data-driven method described in previous sub-section and subtracted it in addition to the combinatorial background. The full calculation is described in Eq. 3.5.

$$S_{+-}(M,p_T) = \begin{cases} N_{+-}(M,p_T) - N^{\mathrm{corr}}_{\pm\pm}(M,p_T) & \text{if } M < M_{\mathrm{th}} \\ N_{+-}(M,p_T) - B^{\mathrm{comb}}_{+-}(M,p_T) \times [1 + r(M,p_T)] & \text{if } M \geq M_{\mathrm{th}} \end{cases} \tag{3.5}$$

where $r(M,p_{\mathrm{T}})$ is the correlated background contribution normalized to the mixed-event combinatorial background. M_{th} is $0.75\,\mathrm{GeV}/c^2$ in our default calculation.

With the background pairs subtracted from the foreground distribution, we were able to obtain the raw signal invariant mass spectrum $S_{+-}(M,p_{\mathrm{T}})$. In the

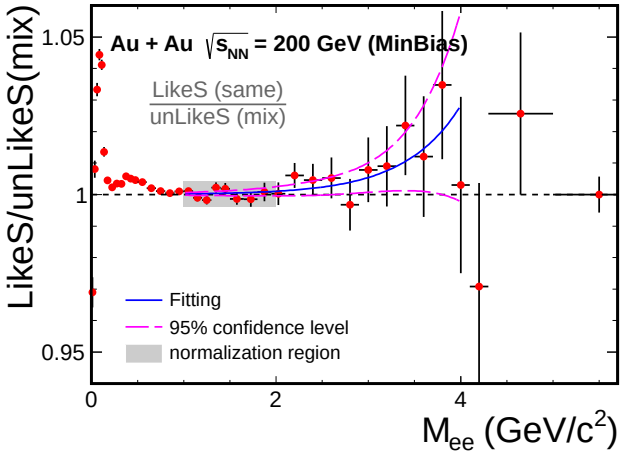

图 3.22: Ratio of the same-event like-sign to the mixed-event unlike-sign distributions. The gray area indicates the normalization region. The solid and dashed lines depict an empirical fit to the distribution in the mass region of $1-4\,\mathrm{GeV}/c^2$ and the fit uncertainties.

upper panel of Fig. 3.25, we show the e^+e^- invariant mass distributions of the same event foreground e^+e^- pairs, the reconstructed background pairs as well as the signal pairs in 200 GeV Au + Au minimum bias collisions. The bottom panel shows the signal-to-background (S/B) ratio in $p+p$ [71] and Au + Au collisions. In Au + Au collisions, the S/B at $M_{ee} = 0.5\,\mathrm{GeV}/c^2$ is about 1/200 in minimum bias and 1/250 in 0-10% central collisions.

3.4 Efficiency and acceptance correction

The obtained raw dielectron signal yields need to correct for the detector efficiency and acceptance loss. In this section, we will discuss the single electron efficiency and electron pair efficiency separately.

3.4.0.1 Single electron efficiency

The single electron efficiency is decomposed into the following terms in this analysis:

$$\varepsilon_e = \varepsilon_{\mathrm{TPC}} \times \varepsilon_{\mathrm{TOF}} \times \varepsilon_{\mathrm{eID}} \tag{3.6}$$

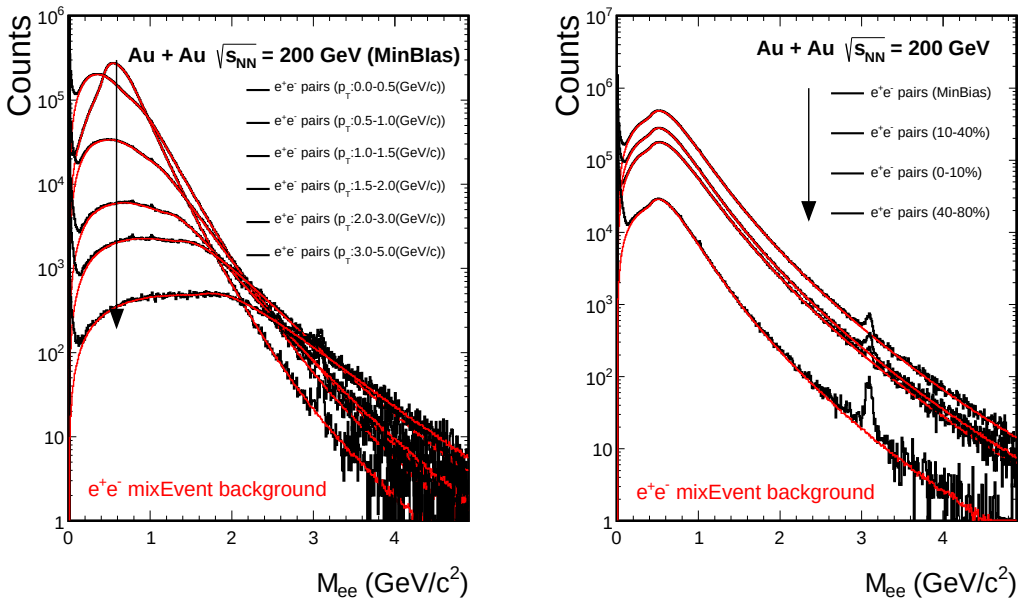

图 3.23: p_T (left) and centrality (right) dependence of the same-event unlike-sign foreground distributions (histograms) and the normalized unlike-sign mixed-event background distributions (red lines).

The TPC tracking efficiency ($\varepsilon_{\rm TPC}$) was evaluated via the standard STAR embedding technique. In the embedding process, MC electron tracks with a certain phase space definition were generated. They were passed into the STAR detector geometry with the year 2010 configuration in the GEANT model [59]. The simulated detector signals were then mixed into the real data with raw signals to have a realistic detector occupancy environment. The mixed signals were processed with the same offline reconstruction software as used for the real data production. The tracking efficiency was studied by comparing the reconstructed tracks with the MC input tracks. The input number of MC tracks were constrained to not to have a sizable impact on the final single tracking efficiency.

The electron track TOF matching efficiency ($\varepsilon_{\rm TOF}$) was obtained from the real data samples. Due to limited pure electron statistics, we firstly used the pure pion sample to deduce the TOF matching efficiency. Pure pions samples

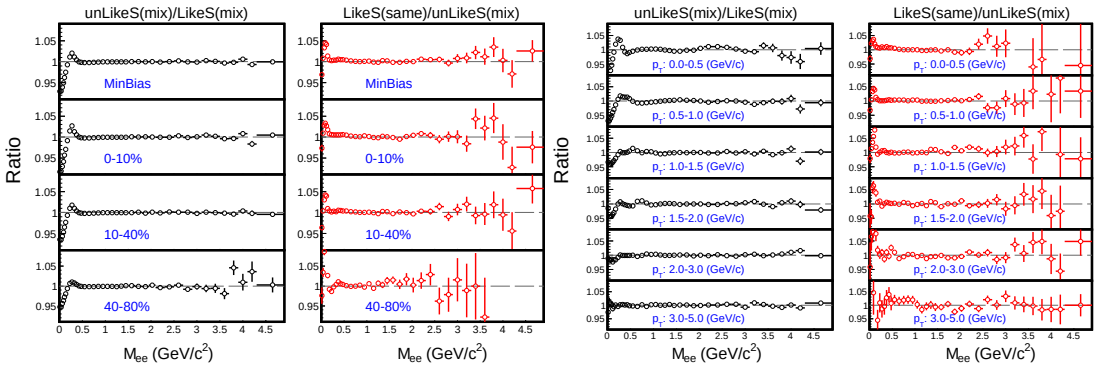

图 3.24: Ratios of unlike-sign to like-sign mixed-event distributions (denoted as the acceptance difference correction factor) and acceptance corrected like-sign background to mixed-event unlike-sign background distributions for different centrality and p_T regions.

were selected by the TPC dE/dx selection and we assume the TOF matching efficiencies for different particle species are the same at the p_T region where dE/dx cannot distinguish different particle species. Pure electron samples were selected to check the efficiency scale difference between electrons and pions due to decay loss of pions between the TPC and the TOF or other effects. Pure conversion electrons were picked up by using the invariant mass reconstruction and also making sure the conversion happened before the track entered into the TPC.

The TPC tracking and TOF matching efficiencies were calculated differentially in three dimensions ($p_{\rm T}$, η, ϕ). The pion TOF matching efficiency has been calculated as well in $p_{\rm T}$, η, ϕ, while we used the same scaling factor for all η, ϕ bins due to limited statistics. The choice of the binning in η, ϕ dimensions show almost a negligible effect in the final dielectron pair efficiency. The upper left panel of Fig. 3.26 shows $\varepsilon_{\rm TPC}$, $\varepsilon_{\rm TOF}$ and their product vs. p_T for $e^{\pm}$ tracks in minimum bias collisions. These efficiency is averaged over $|\eta| < 1$ and 2π in azimuth. The efficiency $\varepsilon_{\rm TPC} \times \varepsilon_{\rm TOF}$ at different centralities (ratios to that in minimum bias collisions) are shown in the bottom left panel of Fig. 3.26.

The electron identification cut efficiency ($\varepsilon_{\rm eID}$) includes two components:

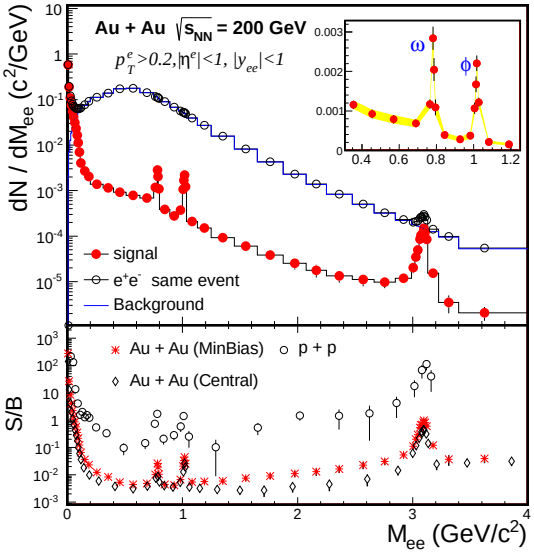

图 3.25: (a): e^+e^- invariant mass pair distributions of signal pairs compared to the raw foreground and reconstructed background pairs in 200 GeV Au + Au minimum bias collisions. The insert show the signal of vector mesons (ϕ, ω). (b): Ratios of signal to background in $p+p$ and Au + Au collisions.

efficiency due to the TOF $1/\beta$ selection cut and efficiency due to the dE/dx PID selection cut.

The dE/dx PID selection cut efficiency includes the efficiency due to the cut on the number of dE/dx points and the efficiency due to the cut on the $n\sigma_e$ to select the final electron candidates. The cut efficiency on the number of dE/dx points was deduced using the pure pion samples in the real data. The result from the photonic electron sample, with much less statistics, shows consistent with that from pions in the region that statistics allows. We then used the one from the pion sample in the final efficiency calculation. The $n\sigma_e$ cut efficiency was deduced via the same step described in the section(electron identification) for calculating the electron purity and hadron contamination. With the extracted $n\sigma_e$ mean position and width values, we then calculated the PID cut efficiency under the selection criteria described before. Figure 3.26 upper right panel shows the each component of PID cut efficiency as well as the total $\varepsilon_{\rm eID}$ as a function of momentum. The centrality dependence of this efficiency is shown in the bottom

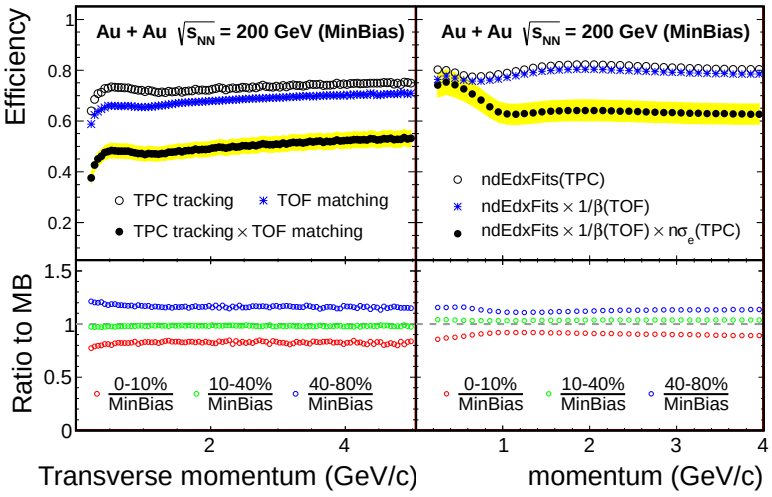

图 3.26: The single electron efficiency as a function of p_T/p in pseudo-rapidity range of $|\eta| < 1$ in Au + Au collisions at $\sqrt{s_{\rm NN}} = 200\,\text{GeV}$. In the left panel the solid point represent the TPC tracking and TOF matching efficiency. In the right panel the solid point show the overall TPC and TOF eID cut efficiency. Yellow bands indicate the systematic uncertainties. The bottom panels show these efficiencies in different centrality bins.

right panel.

3.4.1 Electron pair efficiency and acceptance

Based on the single electron efficiency, we evaluated the dielectron pair efficiency in the following two ways.

- Toy Monte Carlo simulation, which used the virtual photons as the input and let them decay into dielectrons isotropically.
- Cocktail simulation, which used the hadronic cocktail (section: Hadron Cocktail) as input including the correlated heavy flavor decay electrons from PYTHIA simulations [80].

Experimentally we have ambiguities in the final dielectron spectra in determining heavy flavor decayed dielectron yields and medium (including both

hadronic and partonic) produced dielectron yields. Furthermore, the heavy flavor decayed dielectron production is not known in heavy ion collisions due to the possible medium modification on the heavy flavor correlations produced in $p+p$ collisions. We used these two methods to estimate our dielectron pair efficiency, as well as the acceptance extrapolation to full phase space for transverse mass distribution. The single electron efficiency obtained from previous section were folded in for each daughter track in full 3D momentum space. The pair efficiency and acceptance was finally calculated in (M_{ee}, p_{T}).

From the 3D(p_T, η, ϕ) single electron efficiency, we calculated the electron pair efficiency with the two different methods, Fig. 3.27 shows the comparison in different momentum regions within STAR acceptance($p_T^e > 0.2$ GeV/c, $|\eta^e| < 1$, $|y| < 1.0$). We can see there are about 3% difference in the low p_T region, and about 1% difference in the higher p_T region, we took the 3% difference in our systematic uncertainty. Considering the statistics, we used the virtual photon method as the final one.

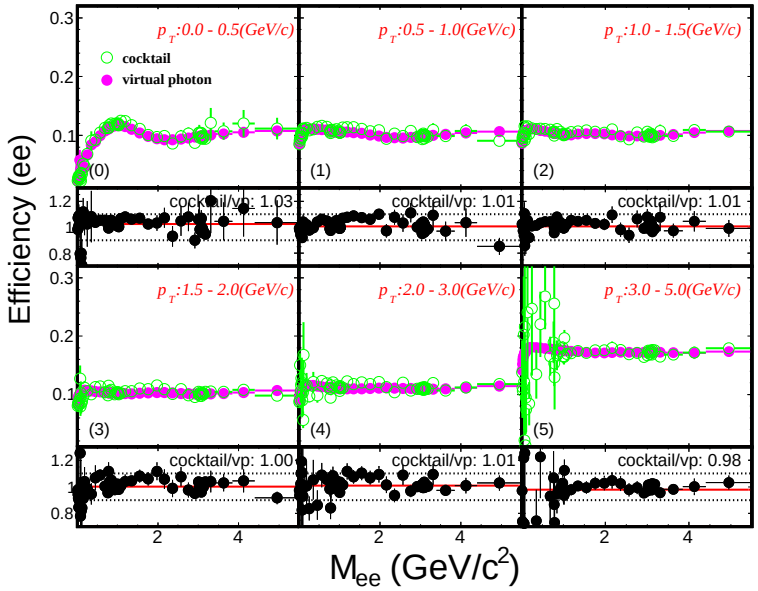

图 3.27: comparison of the efficiency form two different method (virtual photon decay and cocktail)

Fig. 3.28 shows the electron pair efficiency in different momentum regions, we can see in the high momentum region, the pair efficiency are almost flat(as the single electron efficiency is almost flat at high p_T), and in the very low p_T and low mass region the efficiency are almost 0(as the STAR detector acceptance limit). Fig. 3.29 shows the mass dependence of the pair efficiency.

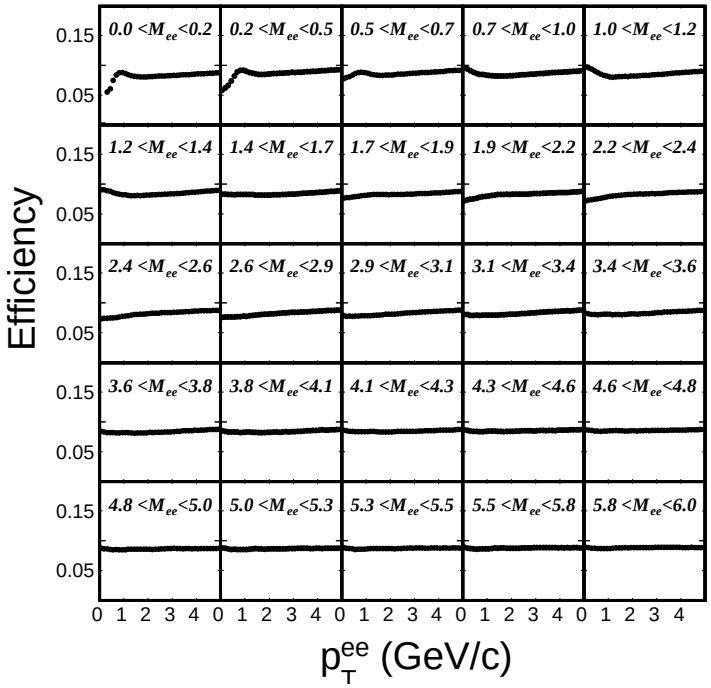

图 3.28: di-electron pair efficiency vs p_T in different mass region for minbias collisions

The results reported here, except for the dielectron transverse mass spectra, are within the STAR acceptance ($p_T^e > 0.2\,\mathrm{GeV}/c$, $|\eta^e| < 1$) and $|y_{ee}| < 1$. To corrected for the STAR acceptance, the dielectron yields within the STAR detector acceptance were further corrected for the acceptance loss for single electrons. The acceptance correction factor ε_{pair}^{acc} is defined as:

$$\varepsilon_{pair}^{acc} = \frac{dN/dM_{ee}dy(p_T(e) > 0.2\mathrm{GeV}/c, |\eta(e)| < 1)}{dN/dM_{ee}dy} \tag{3.7}$$

The dielectron yields are always averaged over $|y_{ee}| < 1$. Figure 3.30 shows the acceptance correction factor from above two methods. The difference in

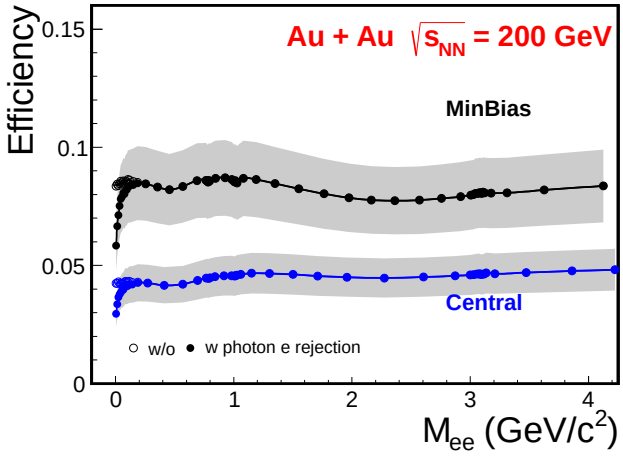

图 3.29: di-electron pair efficiency vs mass for MinBias and Central collision, gray band are the systematic uncertainty

the correlation between decayed daughters in these two methods results in quite different ε_{pair}^{acc}, particularly in the intermediate mass region where the correlated charm contribution becomes a significant factor. Since both the correlation between charm hadron decayed electrons in Au + Au collisions and thermal radiation contribution are unknown, we used the averaged ε_{pair}^{acc} from two methods as our correction factor, and difference between two methods is included in systematic uncertainties. This difference appears to be the largest systematic uncertainty in determining the slope parameter ($T_{\rm eff}$) in the transverse mass spectra.

3.5 Hadronic cocktails

Final state dielectron pairs observed by the detector come from the full time-space evolution of the medium created from collisions. Dielectrons from the decays of long lived particles after they freeze out from the medium will appear in our final extracted signal spectrum. These contributions in the final dielectron spectrum, usually called hadronic cocktails are under control as long as their yields at freeze-out are known.

We performed the similar simulation process for hadronic cocktails in Au + Au collisions as we did in $p+p$ collisions [71]. The cocktail simulation only

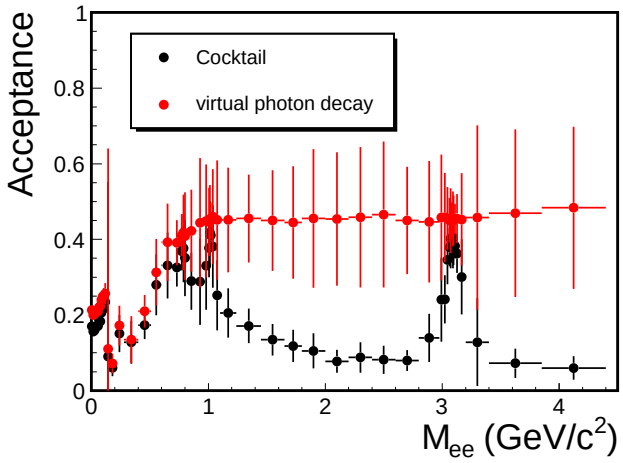

图 3.30: comparison of the acceptance form two different method (virtual photon decay and cocktail)

contains the hadron form-factor decays in the vacuum at freeze-out. Cocktails included in our calculation contain contributions from decays or Dalitz decays of π^0, η, η', ω, ϕ, J/ψ, $c\bar{c}$, $b\bar{b}$ as well as the Drell-Yan (DY) production. We also included a vacuum ρ calculation only when discussing the data compared to cocktails including the vacuum ρ. For hadron decay calculation, the input rapidity distributions were assumed to be flat within $|y| < 1$. The input yields dN/dy within this rapidity window as well as the p_T distributions are discussed below.

The charged pion production yields at 200 GeV Au + Au collisions have been well measured [72, 73]. We took the averaged yield between π^+ and π^- as the input π^0 spectrum. Other available data on input light hadron yields are η from PHENIX but only at $p_{\rm T} > 2\,{\rm GeV}/c$ and ϕ from STAR [77]. These hadron spectra together with other hadron spectra ($K^{\pm}$, K^0_S, Λ) measured by STAR and PHENIX were simultaneously fit to a core-corona based Tsallis Blast-Wave (TBW) model [74] where the core describes the Au + Au bulk production and the corona describes the hard scattering contribution from $p + p$ collisions.

Figure 3.31 shows the simultaneous fit results for all input hadron spectra. The TBW functions provide good parametrization to these measured spectra.

For light hadron cocktail components that don't have measurements (e.g. low p_T η, η', ω), we used the same core TBW parameters obtained from the fit and pre diced the spectra shapes for each of these missing component, shown as dashed curves in Fig. 3.31. The magnitude of the low p_T η spectrum at low p_T was fixed by requiring the match with the measured data points at $p_T > 2\,\mathrm{GeV}/c$, while the dN/dy of η' and ω mesons were taken the same values as used in the PHENIX publication [45].

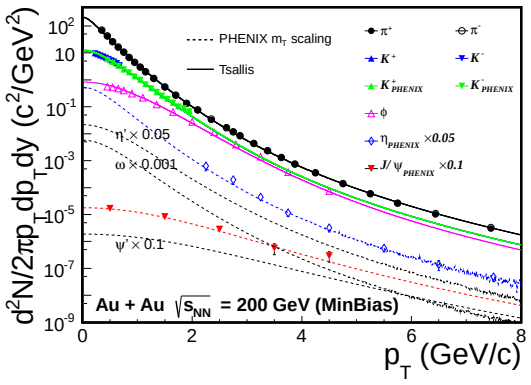

图 3.31: The invariant yield of mesons in Au + Au collisions at $\sqrt{s_{\mathrm{NN}}} = 200\,\mathrm{GeV}$. The solid line show the comparison between the measured data and Tsallis Blast-Wave Fit. The dash line show the comparison between data and m_T scaling (fit parameters from [45]).

Some additional corrections were applied to take into account the differences in centrality and rapidity windows between input hadron spectra and dielectron in this analysis. For instance, the measured pion yields were calculated in the rapidity window of $|y| < 0.1$ in Ref. [72] and $|y| < 0.5$ in Ref. [73]. We used the pion rapidity distribution from the Hijing calculation and scaled the measured pion yields down by 3% to obtain the p_T spectrum in the rapidity window of $|y| < 1$. And this correction factor was also absorbed in the uncertainty of input π^0 dN/dy. Centrality window difference only matters when we take the minimum bias data from PHENIX measurements which were done in 0-92% centrality.

The correlated charm, bottom and Drell-Yan contributions were obtained from PYTHIA calculations [80] and scaled by the number of binary collisions in

表 3.4: Sources of the hadron cocktails.

source	B.R.	dN/dy
$\pi^0 \to \gamma ee$	1.174×10^{-2}	$(9.57 \pm 0.95) \times 10$
$\eta \to \gamma ee$	7×10^{-3}	$(1.08 \pm 0.32) \times 10$
$\eta' \to \gamma ee$	9×10^{-4}	2.05 ± 0.20
$\rho \to ee$	4.72×10^{-5}	9.88 ± 3.00
$\omega \to ee$	7.28×10^{-5}	
$\omega \to \pi^0 ee$	7.7×10^{-4}	8.6 ± 2.8
$\phi \to ee$	2.95×10^{-4}	
$\phi \to \eta ee$	1.15×10^{-4}	2.05 ± 0.60
$J/\psi \to ee$	5.94×10^{-2}	$(1.79 \pm 0.26) \times 10^{-3}$
$c\bar{c} \to ee$	$(1.03 \pm 0.09) \times 10^{-1}$	2.43×10^{-3} (pp)
$b\bar{b} \to ee$	$(1.08 \pm 0.04) \times 10^{-1}$	1.28×10^{-4} (pp)
$DY \to ee$	$(3.363 \pm 0.004) \times 10^{-2}$	1.45×10^{-6} (pp)

Au + Au collisions in the default cocktail calculations. We used the PYTHIA version 6.419 with parameter settings: MSEL=1, PARP(91) ($\langle k_\perp \rangle$) = 1.0 GeV/c and PARP(67) (parton shower level) = 1.0. This setting was tuned to match our measured charmed meson spectrum in $p+p$ collisions [79]. The input charm production cross section in $p+p$ collisions was also taken from the charmed meson measurement:

$$d\sigma^{c\bar{c}}/dy = 170 \pm 45(\text{stat.})^{+38}_{-59}(\text{sys.})\mu b$$

We used the same PYTHIA setting to calculate the dielectron yields from correlated bottom decays and from the Drell-Yan production. The input bottom and Drell-Yan production cross sections are listed in Table. 3.4.

The ρ meson contribution is expected to be modified and considered part of the medium due to the hot QCD medium created in the heavy ion collisions. The ρ meson was not included in our default cocktail calculations. In the comparison between our measured dielectron spectrum to the cocktail calculation including the vacuum ρ, we used the ρ meson measurement in peripheral collisions by STAR

[81] and assumed the same ρ/π ratio to extrapolate to other centrality selections. The mass spectrum of the vacuum $\rho \to e^+e^-$ is chosen as the following function:

$$\begin{aligned}
&\frac{dN}{dm_{ee}dp_T} \propto \frac{m_{ee}M_\rho\Gamma_{ee}}{(M_\rho^2 - m_{ee}^2)^2 + M_\rho^2(\Gamma_{\pi\pi} + \Gamma_{ee}\Gamma_2)^2} \times PS \\
&\Gamma_{\pi\pi} = \Gamma_0 \frac{M_\rho}{m_{\pi\pi}} (\frac{m_{\pi\pi}^2 - 4m_\pi^2}{M_\rho^2 - 4m_\pi^2})^{3/2} \\
&\Gamma_{ee} = \Gamma_0 \frac{M_\rho}{m_{ee}} (\frac{m_{ee}^2 - 4m_e^2}{M_\rho^2 - 4m_e^2})^{1/2} \\
&PS = \frac{m_{ee}}{\sqrt{m_{ee}^2 + p_T^2}} e^{-\frac{\sqrt{m_{ee}^2 + P_T^2}}{T}}
\end{aligned} \tag{3.8}$$

In which M_ρ is 776MeV， M_π is mass of π， Γ_0 is 149MeV， Γ_2 is $\rho \to e + e$ branch ratio， PS is the Boltzmann phase space factor， T $\sim 160MeV$.

Table 3.4 summarize all the possible sources of the hadron cocktails and their decay branching ratios. In the cocktail simulation, we use the Tsallis Blast-Wave [74] or m_T scaling [45] to describe the measured hadron p_T distributions as inputs, shown in Fig.3.31. The products, e^+e^- pair mass distributions from the sources, are normalized by decay branching ratios and the measured dN/dy.

All the following reported mass spectra are not corrected for the STAR detector resolution. It is very challenging to precisely reproduce the momentum resolution in the STAR TPC simulation package under the high luminosity RHIC environment due to various distortion effect in the TPC detector. We used a data-driven method to obtain the dielectron mass line shape in this measurement.

Based the full detector simulation, the reconstructed electron $p_{\mathrm{T}}^{\mathrm{rec}}$ probability distribution at a given input $p_{\mathrm{T}}^{\mathrm{MC}}$ was parameterized with a double-Crystal-Ball function, defined in Eq. 3.9:

$$P(p_{\mathrm{T}}^{\mathrm{rec}}, p_{\mathrm{T}}^{\mathrm{MC}}) \propto \begin{cases} A \times (B - R)^{-n}, & R < -\alpha \\ e^{\frac{-R^2}{2}}, & -\alpha < R < \beta \\ C \times (D + R)^{-m}, & R > \beta \end{cases} \tag{3.9}$$

and

$$
\begin{aligned}
A &= (\frac{n}{|\alpha|})^n \times e^{\frac{-\alpha^2}{2}} \\
B &= \frac{n}{|\alpha|} - |\alpha| \\
C &= (\frac{m}{|\beta|})^m \times e^{\frac{-\beta^2}{2}} \\
D &= \frac{m}{|\beta|} - |\beta| \\
R &= \left(\frac{p_{\mathrm{T}}^{\mathrm{rec}} - p_{\mathrm{T}}^{\mathrm{MC}}}{p_{\mathrm{T}}^{\mathrm{MC}}} - \mu \right) / \frac{\sigma_{p_{\mathrm{T}}}}{p_{\mathrm{T}}}
\end{aligned}
\tag{3.10}
$$

where $n = 1.29$, $\alpha = 1.75$, $m = 2.92$, $\beta = 1.84$.

$\mu = -0.001$ which is slightly shifted due to the electron energy loss in the detector material while the STAR tracking only accounted for the energy loss assuming pion tracks.

$\sigma_{p_{\mathrm{T}}}/p_{\mathrm{T}}$ was used as a measure of the p_T resolution. We fixed all other parameters from the simulation while the p_T resolution was assumed to follow:

$$
(\frac{\sigma_{p_T}}{p_T})^2 = (a \times p_T)^2 + (\frac{b}{\beta})^2; \;\; \beta = \frac{p}{E} \sim \frac{p_T}{\sqrt{p_T^2 + m^2}}. \tag{3.11}
$$

for electrons $\beta \sim 1$.

We then used the J/ψ signal which has the most statistics and tuned the above parameters a and b in the Eq. 3.11 to get the best match to the J/ψ signal distribution. The two parameters were chosen to be $a = 0.0060$ c/GeV and $b = 0.0083$.

3.6 Systematic uncertainty

The major systematic uncertainty sources that contributed to the final result in this analysis include:

1. Conversion electron removal

2. Normalization factor for mixed-event distributions

3. Residual correlated background

4. Like-sign/unlike-sign acceptance difference correction

5. Hadron contamination

6. Efficiency and acceptance correction

Details of the conversion electron remove have been described in pervious Section. Shown previously in Fig. 3.9, to estimate the uncertainty on the final mass spectrum, we compared the results with and without photon conversion removal, and the difference is found to be $< 2\%$ at $M > 0.1\,\mathrm{GeV}/c^2$. We also tried two different conversion removal methods (ϕ_V cut and M cut), and the difference in the final mass spectrum is found to be $< 2\%$ at $M > 0.1\,\mathrm{GeV}/c^2$. Both are included in the point-to-point systematic uncertainties for results above $0.1\,\mathrm{GeV}/c^2$. The uncertainty below $0.1\,\mathrm{GeV}/c^2$ due to this source is dominated by the conversion removal cut efficiency, which will be addressed in the following paragraph on efficiency uncertainties.

The systematic uncertainty on the background of dielectron pairs was also separated in two mass regions where we chose different background subtraction methods (Eq. 3.5).

In the low mass region where $M < 0.75\,\mathrm{GeV}/c^2$, we obtained the signal by subtracting the acceptance corrected like-sign background. The acceptance difference correction was calculated using mixed-event distribution. We chose different event mixing methods by varying the different event categories, event pool size. We took the largest deviation into the uncertainty. The acceptance correction should be done in 2D (M, p_{T}) plane, but may suffer from limited statistics. We took the difference between the results calculated using the 2D acceptance correction and using the 1D (M only) acceptance correction into the systematic uncertainty as well.

In the mass region of $M \geq 0.75\,\mathrm{GeV}/c^2$, we obtained the signal by subtracting the mixed-event unlike-sign background plus the residual correlated background.

表 3.5: Systematic uncertainties on normalization factors of mixed-event distributions for MinBias collisions and various centralities. The total number of e^+e^- pairs in MinBias collisions is $\sim 3.7 \times 10^7$, for Central collisions is $\sim 8.0 \times 10^7$.

	# Like-sign	Choice of N.R.	Norm.Method	LS/US difference	Total
MinBias	5.1×10^{-4}	6.5×10^{-5}	1.0×10^{-4}	2.5×10^{-5}	0.06%
0-10 %	3.2×10^{-4}	1.6×10^{-4}	5.7×10^{-5}	1.6×10^{-5}	0.04%
10-40%	7.9×10^{-4}	6.5×10^{-6}	8.1×10^{-5}	3.3×10^{-5}	0.08%
40-80%	6.9×10^{-4}	6.8×10^{-5}	9.6×10^{-5}	1.0×10^{-4}	0.08%

The normalization of the combinatorial background, the mixed-event unlike-sign distribution is determined by comparing the like-sign same event and mixed-event distributions. The statistics of the total like-sign pair in the normalization region becomes one of the dominate systematic uncertainty. We also chose different normalization ranges varying between the mass range of 1.2 - 2.2 GeV/c^2. Other sources we considered are the normalization method (we chose to normalize the mixed-event unlike-sign directly to the acceptance corrected same event like-sign distribution) and the slight asymmetry between total number of mixed-event unlike-sign and like-sign pairs. Table 3.5 summarizes the contribution of each individual component in Au + Au 200 GeV collisions in minimum bias collisions as well as various centralities. The total systematic uncertainty of the normalization factor was calculated as a direct sum of each individual ones assuming full correlation. The uncertainty in the residual correlated background was already mentioned in pervious section. In the data-driven approach, we counted the statistical uncertainty in determining the ratio of like-sign and mixed-event unlike-sign $r(M, p_{\mathrm{T}})$ as the systematic uncertainty. The contribution to the final dielectron mass spectrum in minimum bias collisions is about 10% from 1 GeV/c to 3 GeV/c.

The electron candidates contain a small amount of contaminated hadrons. If these hadrons were produced with correlation (e.g. resonance decays), they may contribute into the final signal spectrum. To estimate this contribution, we firstly selected the pure pion, kaon and proton samples with stringent TOF

$mass^2$ cuts. We randomly select hadrons from these pure samples according to the estimated hadron contamination levels in both the total amount and the p_T differential yields. Thus we created a hadron candidate pool and performed the same analysis procedure as the dielectron analysis. We estimated the $e-h$ and $h-h$ contribution and compared to the dielectron signal spectrum, shown in Fig. 3.32(left). Overall, the relative contribution to the final spectrum is $< 5\%$ from $1\,\mathrm{GeV}/c$ to $3\,\mathrm{GeV}/c$.

Figure. 3.32(right) summarizes the systematic uncertainties in obtaining the raw dielectron invariant mass spectra for the minimum bias collisions. As a conservative estimation, we took the sum of each individual component as the total systematic uncertainty.

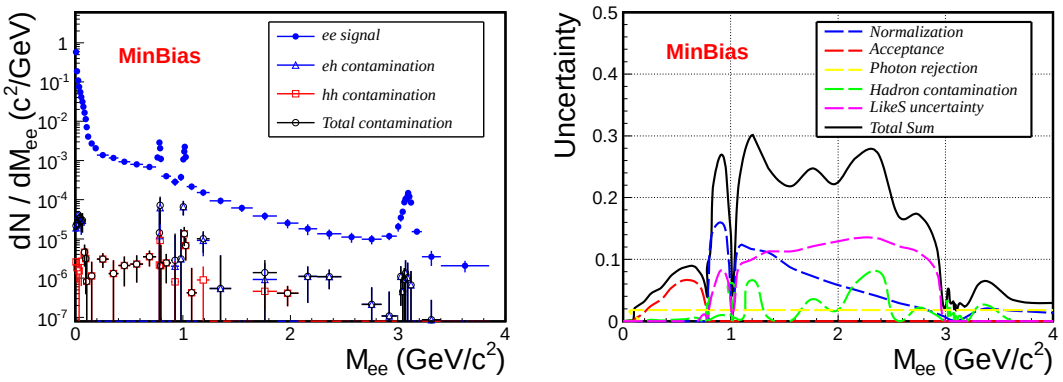

图 3.32: (Left)Hadron contamination estimation, (Right) Systematic uncertainty of dielectron mass spectrum in Au + Au minimum bias collisions.

For the reported dielectron yields in the STAR acceptance, the systematic uncertainty due to the efficiency and acceptance correction includes uncertainties on the single track efficiency, the pair efficiency evaluation method and the pair cut (ϕ_V) efficiency. Table 3.6 summarizes each individual component and their contributions to the total uncertainty of the single track efficiency.

表 3.6: Systematic uncertainties on signal track efficiency

	component	uncertainty
TPC	nHitsFits (diff 15-20)	4.0%
	dca (diff 0.5-1.0 cm)	2.5%
	ndEdxFits	6.0%
TOF	matching	4.2%
	$1/\beta$	3.0%
Total		9.2%

第四章　Results

第五章　Outlook

附录 A　Appendix

A.1　PHENIX acceptance

The STAR mid-rapidity detectors cover full azimuth ($0< \phi < 2\pi$) at $|\eta|$ <1 while the PHENIX central arms (used for the dielectron analysis) cover about $2 \times \pi/2$ at $|\eta| < 0.35$.(Fig. A.1, and Table. A.1). So in principle, STAR can simulate the PHENIX acceptance to study the detector acceptance effect to the dielectron measurements.

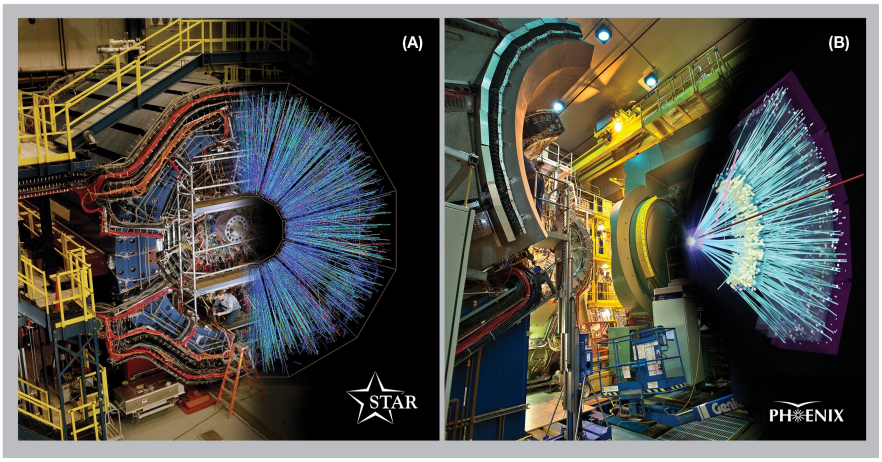

图 A.1: STAR and PHENIX detectors

	ϕ	η	#sector	Tracking	EID
STAR	2π	$\pm 1.$	24	TPC	TPC,TOF,EMC
PHENIX	π	± 0.35	40	DC,PC	RHIC,TOF,EMC

表 A.1: STAR and PHENIX detector acceptance

To investigate the impact of the detector acceptance effect on the final di-electron mass spectrum, we tried to narrow down the single track acceptance cut to match the PHENIX's one as best as we can. We have to acknowledge that there is no way to fully reproduce other experiment's acceptance due to different

detector structures and performances. What we did is to select the STAR data with the PHENIX azimuthal angle acceptance cut. Due to the limited statistics, we cannot further reduce the pseudorapidity window to match the PHENIX's cut. We also considered the physics is not so significantly different between $|\eta| < 0.35$ and $|\eta| < 1$ at 200 GeV collisions.

Due to the existing magnetic field, the signal track ϕ acceptance varies with p_{T}. We used the kinematic acceptance cut presented in the PHENIX publication [45] shown in Eq. A.1:

$$\begin{aligned} \phi_{min} \leq \phi + q\frac{k_{\,DC}}{p_T} &\leq \phi_{max} \\ \phi_{min} \leq \phi + q\frac{k_{RIHC}}{p_T} &\leq \phi_{max} \end{aligned} \tag{A.1}$$

where k_{DC} and k_{RICH} represent the effective azimuthal bend to DC and RICH ($k_{DC} = 0.206$ rad GeV/c and $k_{RICH} = 0.309$ rad GeV/c). One arm covers the region from $\phi_{min} = \text{-}\frac{3}{16}\pi$ to $\phi_{max} = \frac{5}{16}\pi$, the other arm from $\phi_{min} = \frac{11}{16}\pi$ to $\phi_{max} = \frac{19}{16}\pi$.

Figure A.2(left) shows the electron candidate occupancy distributions for our data selected with the PHENIX ϕ acceptance cut. The upper panel shows the regular ϕ vs. p_T for negative charged particles, while the bottom panel shows $1/p_T$ vs. ϕ for both charges. The plot indicates we can capture the basic acceptance structure, while the inner fine structure within this azimuthal angle acceptance may be slightly different due to the detector structure at different experiments.

With the electron candidates selected, we then carried out the same analysis procedure as described before. Figure A.3(right) panel (a), (b), (c) show the ratio of like-sign distributions between same event and mixed-event from which we determined the normalization factor of mixed-event unlike-sign distribution for combinatorial background. Panel (d) shows the acceptance difference correction factor between like-sign and unlike-sign dielectron pairs.

We compared the acceptance difference correction factor between the result with and without the PHENIX ϕ acceptance, shown in Figure A.3. One can

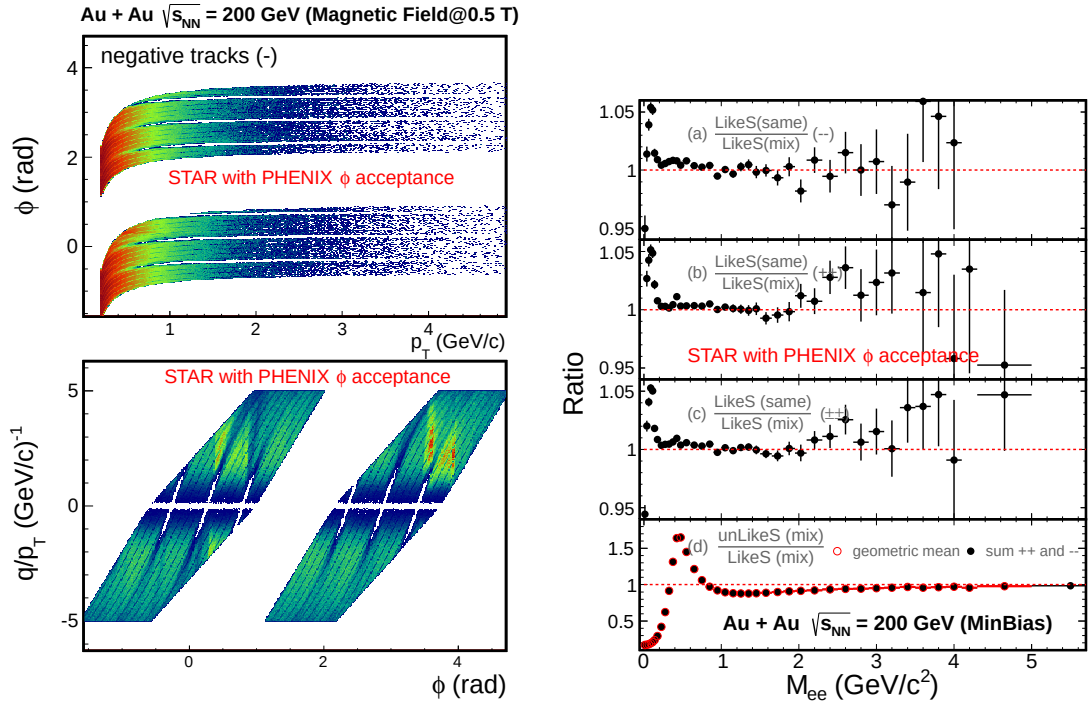

图 A.2: (Left)Single electron/positron track density distributions using the STAR data selected with the PHENIX azimuthal angle acceptance.，(Right)the electron pair mass distribution

clearly see that the ϕ acceptance cut changes the pair acceptance between like-sign and unlike-sign pairs significantly in the low mass region, and the maximum of this ratio happens around $M \sim 0.5\,\mathrm{GeV}/c^2$.

We finished the background subtraction and corrected for the detector efficiency. Finally we obtained the signal dielectron pair invariant mass spectrum from 200 GeV minimum bias Au + Au collisions and compared to hadronic cocktail simulations, shown as the left plot in Fig. A.4. Similarly we observed an enhancement in the low mass region. The enhancement factor is comparable to what we observed with the full azimuthal acceptance.

We further added in the medium dielectron contributions from theoretical model calculations. The right plot of Fig. A.4 shows the data compared with the cocktail plus the broaden ρ spectrum in the hadronic medium and QGP thermal radiation. This particular calculation included here is only valid at $M <$

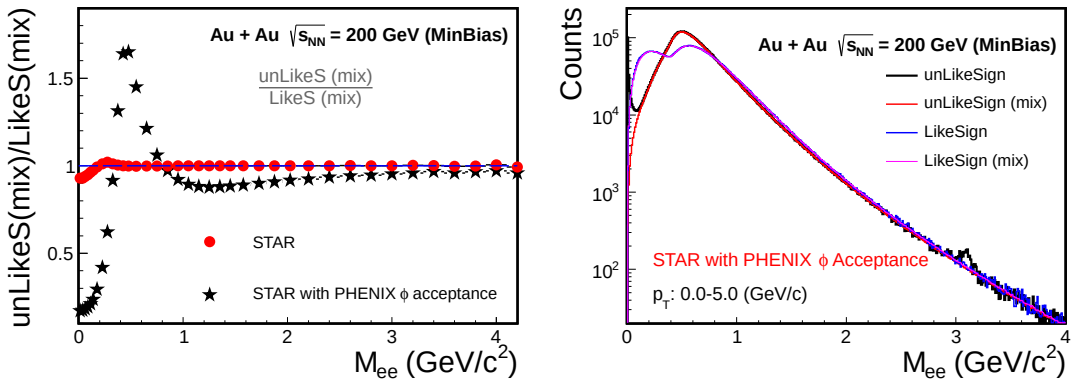

图 A.3: Left Panel: Unlike-sign/like-sign pair acceptance difference correction factor with the PHENIX ϕ acceptance (black stars) compared with the full acceptance(red circles). Right Panel: Dielectron pair mass distributions of the STAR data with the PHENIX ϕ acceptance: the foreground unlike-sign distribution (black), the same event like-sign distribution (blue) and the mixed-event unlike-sign (red), like-sign (magenta) distributions.

1.5 GeV/c^2. We can see that the medium contribution from this model (hadronic ρ and QGP radiation) describes the observed low mass excess very well.

Selecting our data with the PHENIX ϕ acceptance doesn't seem to be able to reproduce the large enhancement factor in the low mass region observed by the PHENIX collaboration [45].

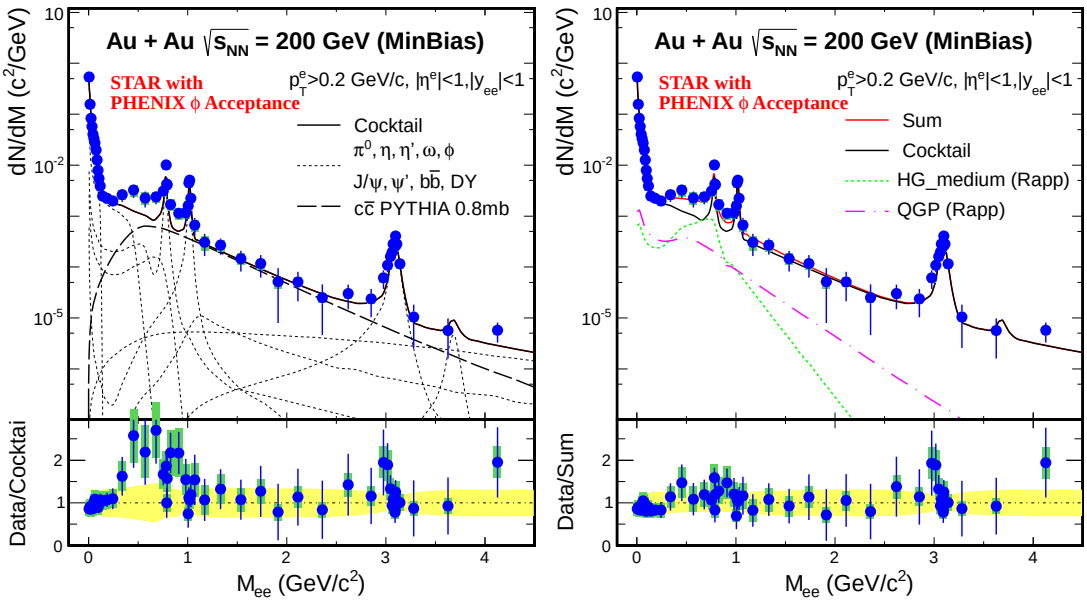

图 A.4: Left: Efficiency corrected invariant mass spectra (blue solid dots) calculated using the STAR data filtered with the PHENIX azimuthal angle acceptance. The data points are compared to cocktail simulations shown as curves and the bottom panel shows the ratio of data to the cocktail sum. Right: The same data points compared to theoretical model calculations of medium vector meson and QGP contributions from Ref. [86]. The bottom panel shows the ratio of data to the sum of the cocktail and the theory calculations of medium contributions.

参考文献

[1] E. V. Shuryak, Phys. Lett. B **78**, 150 (1978).

[2] C. Adler *et al.* Phys. Rev. Lett. **89**, 202301 (2002).

[3] C.-Y. Wong. Introduction to High-Energy Heavy-Ion Collisions. World Scientific Publishing Co. Pte. Ltd., 1994.

[4] F. Wang *et al.* J. Phys. G **30**, S1299 (2004).

[5] John Adams *et al.* Phys. Rev. Lett. **95**, 152301 (2005).

[6] P.F. Kolb and U. Heinz. arXiv: nucl-th/0305084, 2003.

[7] J. Adams et al. "STAR white paper." arXiv: nucl-ex/0501009, 2005.

[8] S.S. Adler *et al.* Phys. Rev. Lett. **91**, 182301 (2003).

[9] J. Adams *et al.* Phys. Rev. Lett. **92**, 052302 (2004).

[10] Z. Lin and C.M. Ko. Phys. Rev. Lett. **89**, 202302 (2002).

[11] D. Molnar and S.A. Voloshin. Phys. Rev. Lett. **91**, 092301 (2003).

[12] J. Adams *et al.* Phys. Rev. Lett. **92**, 052302 (2004).

[13] S. Eidelman *et al.* "Review of Particle Physics." Phys. Lett. B **592**, 1+ (2004).

[14] D. J. Gross and F. Wilczek, Ultraviolet Behavior of Non-Abelian Gauge Theories, Phys. Rev. Lett. **30**, 1343 (1973).

[15] H. D. Politzer, Reliable Perturbative Results for Strong Interactions ?, Phys. Rev. Lett. **30**, 1346 (1973).

[16] D. J. Gross and F. Wilczek, Asymptotically Free Gauge Theories. I, Phys. Rev. D **8**, 3633 (1973).

[17] H. D. Politzer, Asymptotic freedom: An approach to strong interactions, Phys. Rep. 14, 129 (1974).

[18] R. Gupta. arXiv: hep-lat/9807028, 1998.

[19] R. Rapp and J. Wambach. arXiv:hep-ph/9909229v1 2 Sep 1999

[20] 宁平治,李磊,闵德芬. 原子核物理基础-核子与核(高等教育出版社)2002

[21] W.-M. Yao et al., Review of Particle Physics, J. Phys. G **33**, 1 (2006).

[22] J.Goldstone. "Field Theories with Superconductor Solutions." Nuovo Cim.,19:154, 1961.

[23] M. Gell-Mann, R.J. Oakes and B. Renner, Phys. Rev. 175 (1968) 2195.

[24] G. E. Brown and M. Rho, Scaling effective lagrangians in a dense medium, Phys. Rev. Lett. **66**, 2720 (1991).

[25] R. Rapp and J. Wambach, Adv. Nucl. Phys. (Springer, New York, USA, 2000), vol. 25 of Advances in Physics of Particles and Nuclei, chap. Chiral Symmetry Restoration and Dileptons in Relativistic Heavy-Ion Collisions, pp. 1 – 205, ISBN 978-0-306-46440-9, and references therein, Preprint arXiv:hep-ph/9909229.

[26] R. D. Pisarski, Phenomenology of the chiral phase transition, Phys. Lett. B **110**, 155 (1982).

[27] R. J. Porter et al. (DLS Collaboration) Phys. Rev. Lett., 79:1229,

[28] G.Agakishiev et al. (HADES Collaboration) Phys. Rev. Lett 98, 052302

[29] G.Agakishiev et al. (HADES Collaboration) PHYSICAL REVIEW C 84, 014902

[30] G.Agakishiev et al. (HADES Collaboration) PHYSICAL REVIEW C 85, 054005

[31] G.Agakishiev et al. (CERES Collaboration) Phys. Rev. Lett 75, 1272

[32] D.Adamova et al. (CERES/NA45 Collaboration) Phys. Rev. Lett 94, 042301

[33] R. Arnaldi, et al. (NA60 Collaboration) Phys. Rev. Lett 96,162302

[34] R. Arnaldi, et al. (NA60 Collaboration) Phys. Rev. Lett 100,022302

[35] R. Arnaldi, et al. (NA60 Collaboration) Phys. Rev. Lett 102,222301

[36] M. M. Aggarwal et al. (WA98 Collaboration) Phys. Rev. Lett 85, 3595

[37] M. M. Aggarwal et al. (WA98 Collaboration) Phys. Rev. Lett 93, 022301

[38] M. Masera for the HELIOS/3 collaboration,Nuclear Physics A590 (1995)

[39] M. Naruki et al. (KEK-PS E235) Phys. Rev. Lett 96, 092301

[40] G. J. Lolos, et al. (TAGX Collaboration) Phys. Rev. Lett 80, 241

[41] G. J. Lolos, et al. (TAGX Collaboration) PHYSICAL REVIEW C 68, 065202

[42] M. H. Wood et al. (CLAS collaboration) PHYSICAL REVIEW C 78, 015201

[43] M. H. Wood et al. (CLAS collaboration) Phys. Rev. Lett 105, 112301

[44] D. Trnka et al. (CBELSA/TAPS Collaboration) Phys. Rev. Lett 94, 192303

[45] S. S. Adler et al.(PHENIX Collaboration)PHYSICAL REVIEW C 81, 034911

[46] S. S. Adler et al.(PHENIX Collaboration), Centrality Dependence of Direct Photon Production in 200 GeV Au + Au Collisions, Phys. Rev. Lett. 94, 232301

[47] J. Zhao (STAR Collaboration), J. Phys. G 38, 124134 (2011).

[48] M. K. Kohler for the ALICE Collaboration at Hot Quarks2012

[49] A.URAS et al. (ALICE Collaboration) Phys. Lett. B 710 (2012)

[50] Special Issue on RHIC and Its Detectors, edited by M. Harrison, T. Ludlam, and S. Ozaki, Nucl. Instr. Meth. A **499**, No. 2-3 (2003).

[51] M. Anderson, *et al.*, Nucl. Instr. Meth. A **499**, 659 (2003).

[52] S. Eidelman et al. "Review of Particle Physics." Phys. Lett. B **592**, 1+ (2004).

[53] STAR TOF proposal, http://drupal.star.bnl.gov/STAR/files/future/proposals/tof-5-24-2004.pdf.

[54] W.J. Llope, *et al.*, Nucl. Instr. Meth. A **522**, 252 (2004).

[55] M. Beddo, *et al.*, Nucl. Instr. Meth. A **499**, 725 (2003).

[56] C.E. Allgower, *et al.*, Nucl. Instr. Meth. A **499**, 740 (2003).

[57] J. Kyriluk, AIP Conf. Proc. **675**, 424 (2003).

[58] M. Shao *et al.*, Nucl. Instr. Meth. A **614**, 28 (2010).

[59] GEANT 3.21, CERN program library. http://wwwasdoc.web.cern.ch/wwwasdoc/22geanthtml3/geantall.html.

[60] J. Adams *et al.* [STAR Collaboration], Nucl. Phys. A **757**, 102 (2005).

[61] E. Shuryak, Phys. Rep. **61**, 71 (1980).

[62] R. Rapp and J. Wambach, Adv. Nucl. Phys. **25**, 1 (2000).

[63] G.E. Brown and M. Rho, Phys. Rep. **269**, 333 (1996).

[64] R. Rapp and J. Wambach, Eur. Phys. J. A **6**, 415 (1999).

[65] H. van Hees and R. Rapp, Phys. Rev. Lett. **97**, 102301 (2006); H. van Hees and R. Rapp, Nucl. Phys. A **806**, 339 (2008);

[66] J. Ruppert, C. Gale, T. Renk, P. Litchard and J. Kapusta, Phys. Rev. Lett. **100**, 162301 (2008); T. Renk and J. Ruppert, Phys. Rev. C **77**, 024907 (2008);

[67] K. Dusling, D. Teaney and I. Zahed, Phys. Rev. C **75**, 024908 (2007).

[68] O. Linnyk *et al.*, Phys. Rev. C **84**, 054917 (2011).

[69] J. Adams *et al.*, Phys. Lett. B **612**, 181 (2005); J. Adams *et al.*, Phys. Rev. C **71**, 064902 (2005); J. Adams *et al.*, Phys. Rev. Lett. **94**, 062301 (2005).

[70] A.M. Poskanzer and S.A. Voloshin, Phys. Rev. C **58**, 1671 (1998); J. Adams *et al.*, Phys. Rev. C **72**, 014904 (2005).

[71] L. Adamczyk *et al.* [STAR Collaboration], Phys. Rev. C **86**, 024906 (2012).

[72] J. Adams *et al.* [STAR Collaboration], Phys. Rev. Lett. **92**, 112301 (2004).

[73] B.I. Abelev *et al.* [STAR Collaboration], Phys. Rev. Lett. **97**, 152301 (2006).

[74] Z. Tang *et al.*, Phys. Rev. C **79**, 051901 (2009).

[75] S.S. Alder *et al.* [PHENIX Collaboration], Phys. Rev. Lett. **91**, 072301 (2003); S.S. Alder *et al.*, Phys. Rev. C **69**, 034909 (2004).

[76] S.S. Adler *et al.* [PHENIX Collaboration], Phys. Rev. C **75**, 024909 (2007).

[77] J. Adams *et al.* [STAR Collaboration], Phys. Lett. B **612**, 181 (2005).

[78] A. Adare *et al.* [PHENIX Collaboration], Phys. Rev. Lett. **98**, 232301 (2007).

[79] L. Adamczyk *et al.* [STAR Collaboration], Phys. Rev. C **86**, 072013 (2012).

[80] T. Sjostrand *et al.*, Comput. Phys. Commun. **135**, 238 (2001).

[81] J. Adams *et al.* [STAR Collaboration], Phys. Rev. Lett. **92**, 092301 (2004).

[82] C. Amsler *et al.*, Phys. Lett. B **667**, 1 (2008).

[83] V.L. Elestsky *et al.*, Phys. Rev. C **64**, 035202 (2001).

[84] E. Braaten, R.D. Pisarski and T.C. Yuan, Phys. Rev. Lett. **64**, 2242 (1990).

[85] R. Rapp, J. Wambach and H. van Hees, arXiv: 0901.3289.

[86] R. Rapp, private communications.

[87] H.J. Xu *et al.*, Phys. Rev. C **85**, 024906 (2012).

[88] G. Gujanovic *et al.*, arXiv: 1211.0022.

[89] W. Cassing and E.L. Bratkovskaya, Nucl. Phys. A **831**, 215 (2009); E.L. Bratkovskaya, W. Cassing, V.P. Konchakovski, and O. Linnyk, Nucl. Phys. A **856**, 162 (2011).

[90] W. Cassing and E.L. Bratkovskaya, Phys. Rep. **308**, 65 (1999); E.L. Bratkovskaya and W. Cassing, Nucl. Phys. A **619**, 413 (1997); W. Ehehalt and W. Cassing, Nucl. Phys. A **602**, 449 (1996).

[91] O. Linnyk *et al.*, Phys. Rev. C **85**, 024910 (2012).

[92] G. Agakishiev *et al.* [STAR Collaboration], Phys. Rev. Lett. **108**, 072301 (2012).

[93] H. Agakishiev *et al.* [STAR Collaboration], Phys. Rev. D **83**, 052006 (2011).

[94] A. Adare *et al.* [PHENIX Collaboration], Phys. Rev. Lett. **98**, 172301 (2007).

[95] M. He, R.J. Fries and R. Rapp, arXiv: 1204.4442; P.B. Gossiaux *et al.*, arXiv: 1207.5445.

[96] X. Zhu, P. Zhuang, and N. Xu, Phys. Rev. Lett. **100**, 152301 (2008); X. Zhu *et al.*, Phys. Lett. B **647**, 366 (2007).

[97] R. Rapp, Phys. Rev. C **63**, 054907 (2001).

[98] J. Deng, Q. Wang, N. Xu and P. Zhuang, Phys. Lett. B **701**, 581 (2011).

[99] R. Chatterjee, D.K. Srivastava, U. Heinz and C. Gale, Phys. Rev. C **75**, 054909 (2007).

[100] E. Shuryak, arXiv: 1203.1012.

Publication and presentations list

- Publication list:

1. Dielectron continuum production from $\sqrt{s_{NN}}$ = 200 GeV p + p and Au + Au collisions at STAR
   Jie Zhao (for the STAR Collaboration)
   J. Phys. G 38 (2011) 124134
2. Dielectron production from $\sqrt{s_{NN}}$ = 200 GeV Au + Au collisions at STAR
   Jie Zhao (for the STAR Collaboration)
   Nuclear. Physics. A , DOI:10.1016/j.nuclphysa.2012.12.114
3. Elliptic flow of identified hadrons in Au+Au collisions at $\sqrt{s_{NN}}$=7.7-62.4 GeV
   H. Agakishiev et al., (STAR Collaboration)
   e-Print Archives (1301.2348)
4. Observation of an energy-dependent difference in elliptic flow between particles and antiparticles in relativistic heavy ion collisions
   H. Agakishiev et al., (STAR Collaboration)
   Phys. Rev. Lett. 110 (2013) 142301
5. Inclusive charged hadron elliptic flow in Au + Au collisions at $\sqrt{s_{NN}}$=7.7-39 GeV
   H. Agakishiev et al., (STAR Collaboration)
   Phys. Rev. C 86 (2012) 54908
6. Observation of the antimatter helium-4 nucleus
   H. Agakishiev et al., (STAR Collaboration)
   Nature. 473 (2011) 353

- Presentations:

1. Dielectron continuum production from $\sqrt{s_{NN}}$ = 200 GeV p + p and Au + Au collisions at STAR
   XXII International Conference on Ultrarelativistic Nucleus-Nucleus Collisions(Quark Matter 2011), May 23-28, 2011, Annecy, France.
2. Dielectron production from $\sqrt{s_{NN}}$ = 200 GeV Au + Au collisions at STAR
   5th international Conference on Hard and Electromagnetic Probes of High-Energy Nuclear Collisions(Hard Probes 2012), May 27- Jun 1, 2012, Cagliari, Italy.
3. Dielectron production at RHIC
   The second International conference on QCD and Hadron Physics(QCD2013), Mar 29- Apr 2, 2013, Lanzhou, China.

- Publication list 1:

1. Measurement of Charge Multiplicity Asymmetry Correlations 1 in High Energy Nucleus-Nucleus Collisions at 200 GeV
   H. Agakishiev et al., (STAR Collaboration)
   e-Print Archives (1303.0901)
2. Fluctuations of charge separation perpendicular to the event plane and local parity violation in $\sqrt{s_{NN}}$=200 GeV Au+Au collisions at RHIC
   H. Agakishiev et al., (STAR Collaboration)
   e-Print Archives (1302.3802)
3. Freeze-out Dynamics via Charged Kaon Femtoscopy in $\sqrt{(}sNN)$=200 GeV Central Au+Au Collisions
   H. Agakishiev et al., (STAR Collaboration)
   e-Print Archives (1302.3168)
4. System Size Dependence of Transverse Momentum Correlations at RHIC
   H. Agakishiev et al., (STAR Collaboration)
   e-Print Archives (1301.6633)

5. Third Harmonic Flow of Charged Particles in Au+Au Collisions at $\sqrt{s_{NN}}$=200 GeV
   H. Agakishiev et al., (STAR Collaboration)
   e-Print Archives (1301.2187)
6. Measurement of J/ψ Azimuthal Anisotropy in Au+Au Collisions at $\sqrt{s_N N}$=200 GeV
   H. Agakishiev et al., (STAR Collaboration)
   e-Print Archives (arXiv:1212.3304)
7. Studies of di-jets in Au+Au collisions using angular correlations with respect to back-to-back leading hadrons
   H. Agakishiev et al., (STAR Collaboration)
   e-Print Archives (arXiv:1212.1653)
8. J/ψ production at high transverse momenta in p+p and Au+Au collisions at $\sqrt{s_{NN}}$=200 GeV
   H. Agakishiev et al., (STAR Collaboration)
   e-Print Archives (1208.2736)
9. Single Spin Asymmetry A_N in Polarized Proton-Proton Elastic Scattering at $\sqrt{s_{NN}}$=200 GeV
   H. Agakishiev et al., (STAR Collaboration)
   Phys. Lett. B 719 (2013) 62
10. Transverse Single-Spin Asymmetry and Cross-Section for π^0 and η Mesons at Large Feynman-x in Polarized p+p Collisions at $\sqrt{s}$=200 GeV
    H. Agakishiev et al., (STAR Collaboration)
    Phys. Rev. D 86 (2012) 51101
11. Longitudinal and transverse spin asymmetries for inclusive jet production at mid-rapidity in polarized p+p collisions at $\sqrt{s_{NN}}$=200 GeV
    H. Agakishiev et al., (STAR Collaboration)
    Phys. Rev. D 86 (2012) 32006
12. Measurements of D^0 and D^* Production in $p + p$ Collisions at $\sqrt{s}$=200 GeV

H. Agakishiev et al., (STAR Collaboration)
Phys. Rev. D 86 (2012) 72013

13. Di-electron spectrum at mid-rapidity in $p + p$ collisions at $\sqrt{s}$=200 GeV
H. Agakishiev et al., (STAR Collaboration)
Phys. Rev. C 86 (2012) 24906

14. Hadronic Trigger using electromagnetic calorimeter and particle identification at high-pT with STAR Detector
H. Agakishiev et al., (STAR Collaboration)
e-Print Archives (1112.2946)

15. Directed Flow of Identified Particles in Au + Au Collisions at $\sqrt{s_{NN}}$=200 GeV at RHIC
H. Agakishiev et al., (STAR Collaboration)
Phys. Rev. Lett. 108 (2012) 202301

16. Measurement of the $\boldsymbol{W \to e\nu}$ and $\boldsymbol{Z/\gamma^* \to e^+e^-}$ Production Cross Sections at Mid-rapidity in Proton-Proton Collisions at $\boldsymbol{\sqrt{s}}$=500 GeV
H. Agakishiev et al., (STAR Collaboration)
Phys. Rev. D 85 (2012) 92010

17. Energy and system-size dependence of two- and four-particle v_2 measurements in heavy-ion collisions at 62.4 and 200 GeV and their implications on flow fluctuations and nonflow
H. Agakishiev et al., (STAR Collaboration)
Phys. Rev. C 86 (2012) 0

18. Energy and system-size dependence of two- and four-particle v_2 measurements in heavy-ion collisions at 62.4 and 200 GeV and their implications on flow fluctuations and nonflow
H. Agakishiev et al., (STAR Collaboration)
Phys. Rev. C 86 (2012) 0

19. System size and energy dependence of near-side dihadron correlations
H. Agakishiev et al., (STAR Collaboration)
Phys. Rev. C 85 (2012) 14903

20. Identified Hadron Compositions in p+p and Au+Au Collisions at High Transverse Momenta at $\sqrt{s_{NN}}$= 200 GeV
    H. Agakishiev et al., (STAR Collaboration)
    Phys. Rev. Lett. 108 (2012) 72302
21. Directed and elliptic flow of charged particles in Cu+Cu collisions at $\sqrt{s_{NN}}$=22.4 GeV
    H. Agakishiev et al., (STAR Collaboration)
    Phys. Rev. C 85 (2012) 14901
22. ρ^0 photoproduction in Au+Au collisions at $\sqrt{s_{NN}}$=62.4 GeV measured with the STAR detector
    H. Agakishiev et al., (STAR Collaboration)
    Phys. Rev. C 85 (2012) 14910
23. Strangeness Enhancement in Cu+Cu and Au+Au Collisions at $\sqrt{s_{NN}}$=200 GeV
    H. Agakishiev et al., (STAR Collaboration)
    Phys. Rev. Lett. 108 (2012) 72301
24. Evolution of the differential transverse momentum correlation function with centrality in Au + Au collisions at $\sqrt{s_{NN}}$=200 GeV
    H. Agakishiev et al., (STAR Collaboration)
    Phys. Lett. B 704 (2011) 467
25. Experimental studies of di-jet survival and surface emission bias in Au+Au collisions via angular correlations with respect to back-to-back leading hadrons
    H. Agakishiev et al., (STAR Collaboration)
    Phys. Rev. C 83 (2011) 061901
26. High pT nonphotonic electron production in p+p collisions at $\sqrt{s_{NN}}$=200 GeV
    H. Agakishiev et al., (STAR Collaboration)
    Phys. Rev. D 83 (2011) 052006
27. Strange and multistrange particle production in Au + Au collisions at $\sqrt{s_{NN}}$=62.4 GeV

M. M. Aggarwal et al., (STAR Collaboration)
Phys. Rev. C 83 (2011) 024901

28. Measurement of the Parity-Violating Longitudinal Single-Spin Asymmetry for $W^{\pm}$ Boson Production in Polarized Proton-Proton Collisions at $\sqrt{s_{NN}}$=500 GeV
M. M. Aggarwal et al., (STAR Collaboration)
Phys. Rev. Lett. 106 (2011) 062002

29. Scaling properties at freeze-out in relativistic heavy-ion collisions
M. M. Aggarwal et al., (STAR Collaboration)
Phys. Rev. C 83 (2011) 034910

30. Measurement of the Bottom Quark Contribution to Nonphotonic Electron Production in p+p Collisions at $\sqrt{s_{NN}}$=200 GeV
M. M. Aggarwal et al., (STAR Collaboration)
Phys. Rev. Lett. 105 (2010) 202301

31. K^{*0} production in Cu+Cu and Au+Au collisions at $\sqrt{s_{NN}}$=62.4 GeV and $\sqrt{s_{NN}}$=200 GeV
M. M. Aggarwal et al., (STAR Collaboration)
Phys. Rev. C 84 (2011) 34909

32. Balance functions from Au+Au, d+Au, and p+p collisions at $\sqrt{s_{NN}}$=200 GeV
M. M. Aggarwal et al., (STAR Collaboration)
Phys. Rev. C 82 (2010) 024905

33. Higher Moments of Net Proton Multiplicity Distributions at RHIC
M. M. Aggarwal et al., (STAR Collaboration)
Phys. Rev. Lett. 105 (2010) 022302

34. Azimuthal di-hadron correlations in d+ Au and Au + Au collisions at $\sqrt{s_{NN}}$=200 GeV measured at the STAR detector
M. M. Aggarwal et al., (STAR Collaboration)
Phys. Rev. C 82 (2010) 024912

35. Pion femtoscopy in p+p collisions at $\sqrt{s_{NN}}$=200 GeV M. M. Aggarwal

et al., (STAR Collaboration)
Phys. Rev. C 83 (2011) 64905

36. Longitudinal scaling property of the charge balance function in Au+Au collisions at $\sqrt{s_{NN}}$=200 GeV
B.I. Abelev et al., (STAR Collaboration)
Physics Letters B. Vol 690 (2010) 239

37. Charged and strange hadron elliptic flow in Cu+Cu collisions at $\sqrt{s_{NN}}$= 62.4 and 200 GeV
B.I. Abelev et al., (STAR Collaboration)
Phys. Rev. C 81 (2010) 44902

38. Upsilon cross section in p+p collisions at $\sqrt{s_{NN}}$=200 GeV
B.I. Abelev et al., (STAR Collaboration)
Phys. Rev. D 82 (2010) 12004

39. Three-Particle Coincidence of the Long Range Pseudorapidity Correlation in High Energy Nucleus-Nucleus Collisions
B.I. Abelev et al., (STAR Collaboration)
Phys. Rev. Lett. 105 (2010) 22301

40. Inclusive pi^0, η, and direct photon production at high transverse momentum in p+p and d+Au collisions at $\sqrt{s_{NN}}$=200 GeV
B.I. Abelev et al., (STAR Collaboration)
Phys. Rev. C 81 (2010) 64904

41. Observation of $\pi^+\pi^-\pi^+\pi^-$ photoproduction in ultraperipheral heavy-ion collisions at $\sqrt{s_{NN}}$=200 GeV at the STAR detector
B.I. Abelev et al., (STAR Collaboration)
Phys. Rev. C 81 (2010) 44901

42. Spectra of identified high-p_T $\pi^{\pm}$ and $\bar{p}$ in Cu + Cu collisions at $\sqrt{s_{NN}}$=200 GeV
B.I. Abelev et al., (STAR Collaboration)
Phys. Rev. C 81 (2010) 54907

43. Longitudinal double-spin asymmetry and cross section for inclusive

neutral pion production at midrapidity in polarized proton collisions at $\sqrt{s_{NN}}$=200 GeV
B.I. Abelev et al., (STAR Collaboration)
Phys. Rev. D 80 (2009) 111108

44. Observation of an Antimatter Hypernucleus
B.I. Abelev et al., (STAR Collaboration)
Science 328, 58-62 (2010)

45. Longitudinal spin transfer to Lambda and Lambda hyperons in polarized p+p collisions at $\sqrt{s_{NN}}$=200 GeV
B.I. Abelev et al., (STAR Collaboration)
Phys. Rev. D 80 (2009) 111102

46. Identified particle production, azimuthal anisotropy, and interferometry measurements in Au+Au collisions at $\sqrt{s_{NN}}$=9.2 GeV
B.I. Abelev et al., (STAR Collaboration)
Phys. Rev. C 81 (2010) 24911